Design and Development of Dual-Band Integrated Network Analyzer For Water Solvent Based RF Bio Sensors

Thesis submitted in partial fulfillment
of the requirements for the degree of

Master of Science
in
Electronics and Communication Engineering
by Research

by

MAYANK AWASTHI
2018702010
mayank.awasthi@research.iiit.ac.in

International Institute of Information Technology
Hyderabad - 500 032, INDIA
January 2023

International Institute of Information Technology
Hyderabad, India

CERTIFICATE

It is certified that the work contained in this thesis, titled "Design and Development of Dual-Band Integrated Network Analyzer For Water Solvent Based RF Bio Sensors " by Mayank Awasthi, has been carried out under my supervision and is not submitted elsewhere for a degree.

Date	Adviser: Dr. Syed Azeemuddin
Date	Co-Adviser: Dr. M. Hashmi

To Family and Friends

Acknowledgements

Firstly, I would like to express my gratitude towards my advisor Dr. Syed Azeemuddin and my co-advisor Dr. Mohammad S Hashmi for providing me the opportunity to work on this thesis. They have always encouraged and motivated me to understand the physical meaning of each principle used in the research work. This thesis would not have been possible without their constant support, guidance, encouragement and motivation.

The Covid-19 pandemic really affected everyone and we were not the exceptions. However, the flexibility that has been provided to me to do research from home was one the of the things that I will be grateful for. I would really like to thanks once again Dr. Syed and Dr. Hashmi for having the their faith in me and directing me to learn and try new things that helped me in my research and personal life.

I am thankful to my parents and family for their love and support throughout the research. They were always there for me in my ups and downs.

My sincere thanks to Ojas Med Tech Lab for providing me access to the labs equipment and conducting my experiments there.

I am thankful to my all CVEST lab mates, for all the late-night discussions which has helped me grow. I also like to thank all my friends Sumana Bhattacharjee, Muskan Singla, Annesha Mazumdar,Prasenjit Saha, Kunal Wadhwani, Vrushali Arute and juniors for all their support during my journey.

I would like to thank IIIT Hyderabad for providing me with such a beautiful campus with amazing research culture and facilities. Moreover, discussions in the mess on diverse topics and sports helped me reduce stress and maintain a healthy work and life balance.

Finally, I would like to thank God for giving me this life and the opportunity to work with some of the amazing minds and add some value to our scientific community. Thanks to all the people who were with me during my journey in IIIT-H.

Abstract

The detection of analytes using Radio Frequency (RF) based sensors has gained immense popularity in recent times. The change in the sensor's resonant frequency in the presence of different analytes is used as the basis for detection. Although, there have been plethora of advancements in developing RF biosensors, yet most of them have been designed and fabricated considering air all around them. However, in a practical scenario, a solute is mostly used with solvent for testing. The solvent alone produces huge shift in resonant frequency whereas, the shift due to solute and solvent together is significantly narrower (in MHz) when compared to the solvent alone. This indicates that the shift due to solute is narrowband in nature. Most of these sensors utilize traditional Vector Network Analyzers (VNAs) for measuring the s-parameters. However, traditional VNAs are broadband devices that are expensive, large and cumbersome to operate. These VNAs also have much larger bandwidths than the observed frequency shifts as mentioned above and often prove to be overkill. Thus, the optimal solution is to develop narrowband measurement platforms that precisely monitor the frequency shifts. This article tackles the challenge and presents a solvent specific integrated solution for the detection of materials having different permittivities. An Integrated Biosensing Network Analyser (IBNA) is designed and fabricated using microstrip line technology to detect different analytes (Glucose and Sucrose). IBNA primarily consists of a sensing and a measuring unit specifically designed for solvent like water. While the Interdigitated Capacitor based RF Bio Liquid Cavity resonating at 2.3 GHz performs the sensing operation, the Dual Band Six-Port Reflectometer (DBSPR), with an operating frequency of 1.1 GHz and 2.3 GHz, participates in the measurement of the s-parameters. Furthermore, to demonstrate the working of the design, the detection of 1 M Glucose and Sucrose is performed by EM-simulations and experiments. The sensing is carried out efficiently, with Glucose and Sucrose yielding frequency shifts of 15 MHz and 20 MHz at room temperature respectively. The results help in establishing the utility of IBNA and its superiority over traditional network analyzers.

Contents

List of Figures

List of Tables

Chapter 1

Introduction

This chapter provides an overview and past developments in the field of Radio Frequency (RF) Bio chemical sensing. The chapter explains how the traditional VNAs that are being used for measuring necessary parameter for the RF Bio chemical sensor proves to be an overkill. The subsequent sections provides the details of the proposed solutions, the need for six port reflectometer, contribution to this thesis and thesis organisation.

1.1 RF Bio Sensing

Over the last two decades, RF based sensing has successfully captured the scientific community's attention and become a focal point in material characterisation research. The technique's numerous advantages contribute to its widespread use across a wide range of industries. The detection method is low-cost, quick, simple, portable, and robust. It is also simple to integrate with existing IC technology.

In recent years, RF sensing has shown tremendous promise in biochemical sensing. It is currently being investigated for a variety of applications, including bioliquid characterisation, biomolecule analysis [1–3], pathogen detection [4–6], cell analysis [7–13] and nanostructure characterisation [14, 15].

The detection methodology focuses on the variation in the sensor's scattering parameters (s-parameters) in the presence of various Materials Under Test (MUT). Interdigitated Capacitors, Coplanar Waveguides, and Split Ring Resonators are all common RF sensors.The s-parameters can be calculated using some network analysis techniques. Otherwise, Vector Network Analysers (VNAs) are used for measuring the s-parameters.

1.2 Microwave Network Analyser

Microwave network measurements are the foundation of microwave technology. A microwave network analyser is a computer-controlled automated measurement system that includes a synthesizer source, a test-set, a receiver, as well as processing and display units. The network analyser includes the directional couplers and switches needed to measure one or two-port networks. Figure 1.1 depicts the main components of a VNA. A two-port's [S] parameters matrix measurement necessitates two dis-

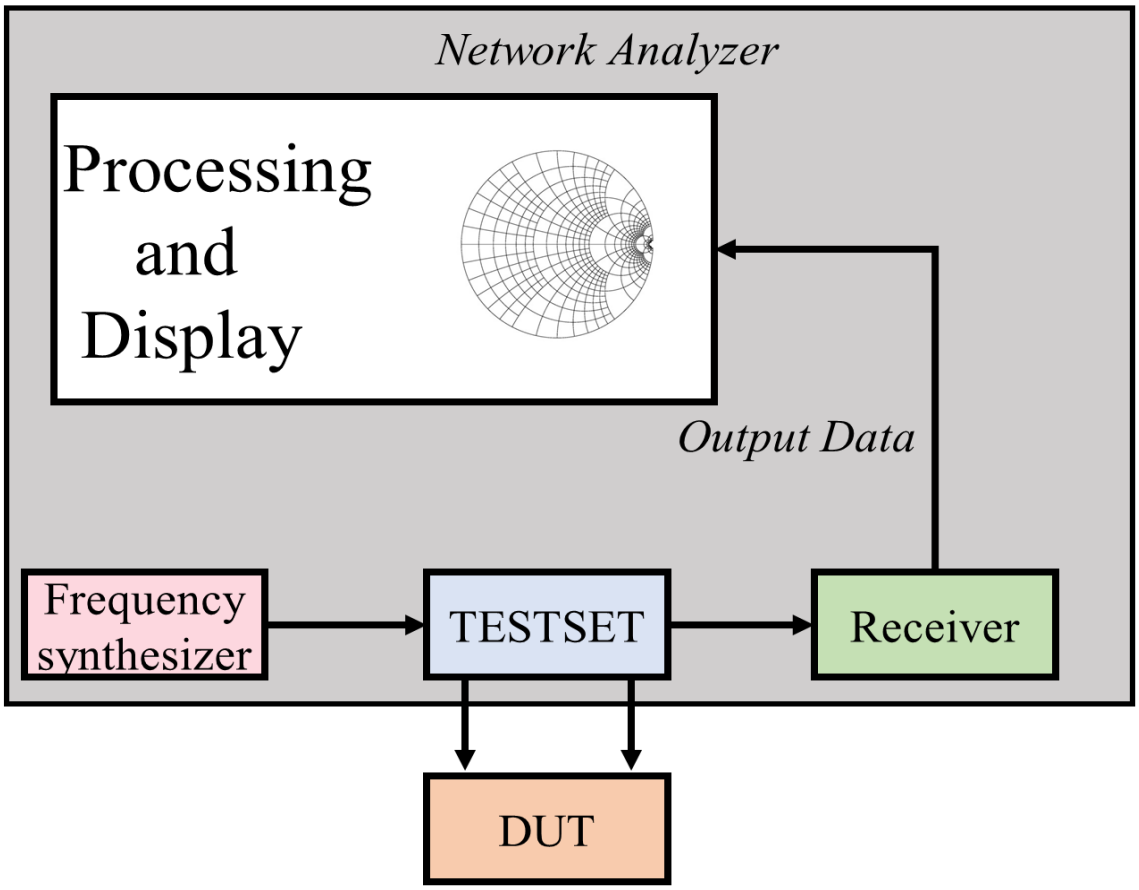

Figure 1.1 Basic architecture of a conventional vector network analyser

tinct setups [16]. The basic network analyser has three RF input ports and an RF source with Z_0 output impedance (characteristic and line impedance).

A detection system that gives simultaneous amplitude and phase responses is essential for the deployment of a VNA. The detecting component is often implemented using a heterodyne design that includes several frequency conversions and local oscillators. The measurement structure is fairly com-

plex and expensive.

1.3 Motivation

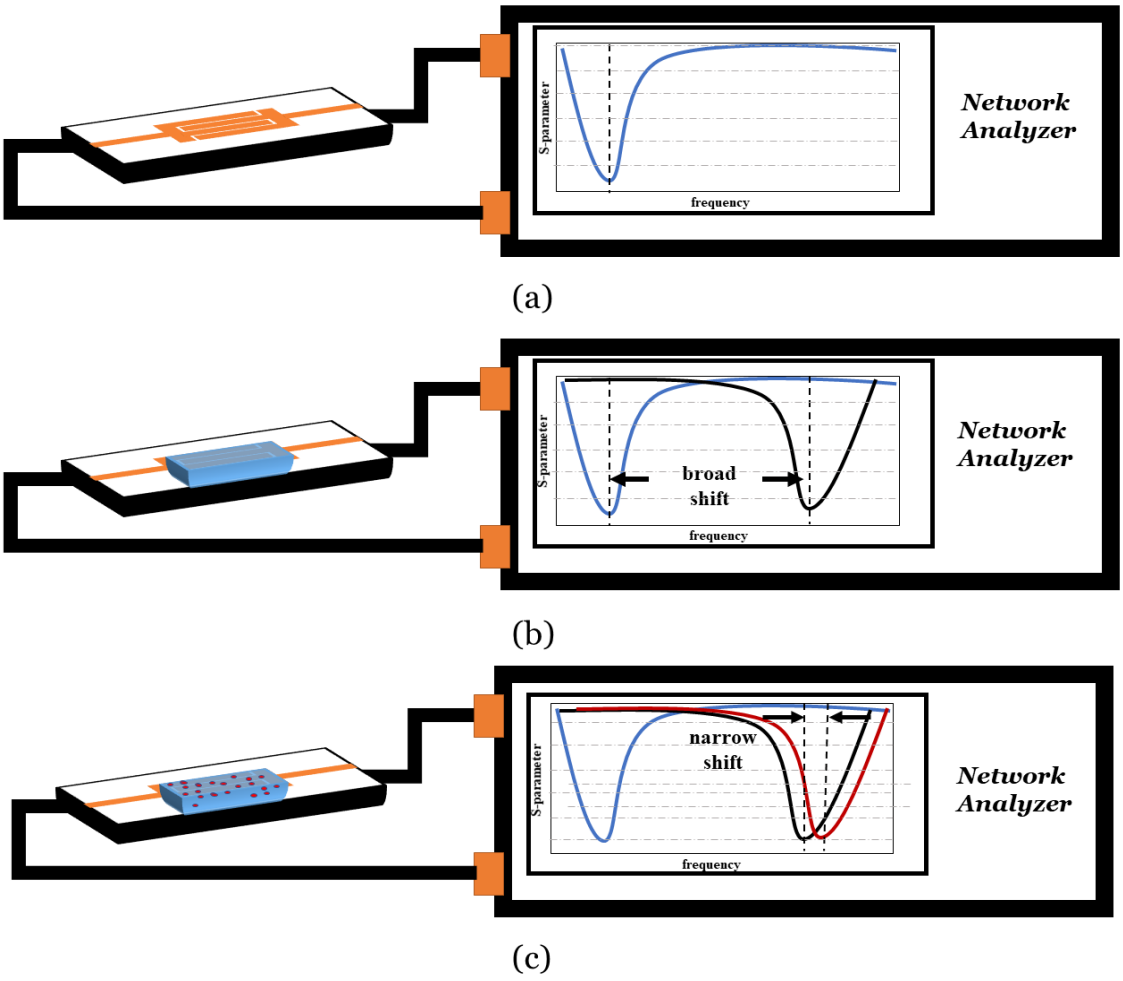

Figure 1.2 Shift in frequency at different stages (a) empty RF biosensor, (b) solvent over RF biosensor, and (c) mixture of solvent and solute over RF biosensor.

A typical RF-based sensing experimental setup consists of an RF sensor connected to a VNA for measuring the s-parameters. However, in most of these reports [17–19] the RF sensor was designed and manufactured with air-filled cavities in mind. This complicates the design and analysis procedure because, in most practical scenarios, samples are dissolved in solvents such as water, ethanol, and phosphate buffer before being tested. Furthermore, when compared to air, these solvents have a high per-

mittivity. This results in very high resonance frequency shifts, as can be seen from equations 1.1 and 1.2.

$$f = \frac{1}{(2\pi\sqrt{LC})} \tag{1.1}$$

$$C = \epsilon.\frac{A}{d} \tag{1.2}$$

where, f, L and C denotes the resonant frequency, equivalent inductance and capacitance respectively. ϵ, A and d have there usual meanings.

In general, resonance frequency shifts caused by solvents with respect to air are in the GHz range. However, in most practical cases, after the addition of solute in solvent the change in the dielectric constant is minor which results in a narrow shift in resonant frequency (in the MHz range). This indicates that the shift due to solute is narrowband in nature as indicated in Fig. 1.2. Most of these sensors utilise traditional VNAs for measuring the s-parameters. However, traditional VNAs are broadband devices that are expensive, large and cumbersome to operate. These VNAs also have much larger bandwidths than the observed frequency shifts as mentioned above and often prove to be an overkill. This demonstrates the need for a narrowband solvent-specific device capable of measuring the shift in resonant frequency caused by a change in the solute. Furthermore, in order to meet the challenges posed by traditional VNAs, the device must be portable and affordable.

1.4 Six Port Reflectometer and its need

There have been several previous attempts to design measurement setups for analysing S-parameters. The reflectometer mentioned in [20] operates at a frequency of 2.4 GHz and utilises AD8302 to measure the reflection coefficient. However, the AD8302 contains mixers and log amplifiers, which complicate the designing process. The high frequency wideband 4 - 32 GHz VNA design in [21], looks interesting. However, it consists of multi-channel receivers, Low Noise Amplifiers (LNA), and micro mixers for the down-conversion of signals. The presence of the complex structure may constrain the design process, may be prone to errors and can turn out to be cost-ineffective. Furthermore, another VNA in [22] was designed using a heterodyne architecture that operates at 50-100GHz. Although the structure looks promising, the operating frequency was way too much to be utilised for biosensors like Complimentary Split Ring Resonator (CSRR),and Inter Digitated Capacitors (IDCs) in biosensing applications.

To tackle the above issues, a Six-Port Reflectometer (SPR) was designed [23–25] to measure the magnitude and phase of reflected power. However, the device operates at a frequency of 10 GHz and utilises waveguide components, making it large and bulky. Moreover, the operating frequency is so high that it has limited bio-sensing applications.

The SPR uses additional detectors to provide a low-cost measurement of both amplitude and phase. Furthermore, the six-port can perform power measurements in addition to network parameters. The name six-port derives from the accompanying network, where these power detectors are used to terminate four of the ports while the remaining two offer connections to the signal source and test port [26].

The six-port allows for simultaneous power flow and impedance measurements using only amplitude measurements, with no need for phase measurements. Using one or two six-ports in combination with an appropriate test-set and measurement procedure, the four scattering parameters of any two-port DUT can be determined [27].

A Tri-band SPR was also designed and fabricated as a prominent solution for the earlier problems in [28]. It utilises the periodic nature of microstrip lines to produce the rest of the two bands, which are the harmonics of the fundamental frequency. This restricts the design and application of the device to certain frequencies only. Therefore, a six-port reflectometer designed for specific frequencies would be a better solution.

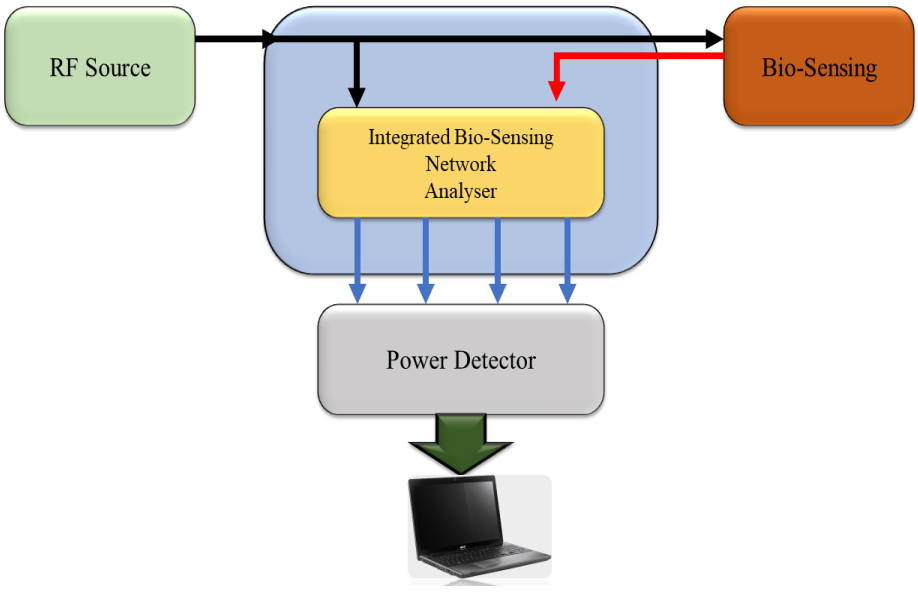

Figure 1.3 Basic Block diagram of proposed dual-band integrated network.

1.5 Contribution of this thesis

This work presents an Integrated Biosensing Network Analyzer (IBNA) that is specifically designed to detect a shift in resonant frequency at two different arbitrary frequencies. A Dual-Band Six-Port Reflectometer (DBSPR) and an RF Bio-Liquid Cavity are also designed and included in the device. The device's dual-band nature does not rely on the periodic behaviour of transmission lines hence extending its reach for practical applications. Furthermore, its superiority over traditional VNAs in measuring the shift in resonance frequency is enhanced by its impressive power handling capability, small size, low cost, and lightweight nature. Fig. 1.3 shows basic block diagram of proposed dual band Integrated Bio-Sensing Network Analyser. A detailed analysis and designing process of IBNA will be covered in the subsequent chapters.

1.6 Thesis Organisation

This section gives a brief description of the structure of the thesis.

Chapter 2 presents microwave network theories and fabrication technologies that are currently being used. It also introduces different terminologies and microwave passive devices.

Chapter 3 provides an overview of how to design a dual band coupler. The chapter presents the process of designing a dual band coupler using NI AWR. It also discusses popular works involving different designing techniques aimed at aiding designing of microstrip line couplers.

Chapter 4 addresses the process of designing a dual band power divider. It presents the designing process, simulation results and demonstrate the relevance of process using s-parameters.

Chapter 5 highlights the designing of Integrated Bio-Sensing Network Analyser by integrating couplers, power divider and RF-Bio Liquid Cavity (bio sensor) in specific manner such that the overall structure is able to measure the shift in frequency for s_{11} and s_{21} parameters. Furthermore, simulations using 3D EM simulator CST, mimicking placement of different materials with varying dielectric constant has also been performed and results were displayed in Results section.

Finally, in conclusion, we summarise our finding along with the possible future directions and possibilities.

Chapter 2

Microwave Network Theory and Fabrication Technologies

This chapter briefly explains the fundamental concepts and principles related to microwave network theory, transmission lines, scattering matrix, microwave passive circuits like directional couplers and power dividers, microwave fabrication technologies, six port circuit, RF bio sensing and network analyser.

2.1 Microwave Network Theory

The calculation and measurement of voltages and currents for non-TEM lines is not straightforward task [29]. Moreover, there are some practical limitations when one tries to measure voltages and currents in microwave frequencies. To remedy these problems, the incident and reflected powers and their parameters are measured in microwave frequencies. The scattering parameters, which indeed are the parameters that can be directly related to power measurements, are used to characterise microwave circuits and networks.

2.1.1 Power and Reflection

This section presents the concepts for the calculation of reflected power. Figure 1.1 shows a one-port network with impedance Z that is connected to the generator with generator impedance Z_g. Power is transmitted from the generator to the one-port network. The current and voltage at terminal are

$$i = \frac{V_g}{Z_g + Z_l} \tag{2.1}$$

and

$$v = \frac{ZV_g}{Z_g + Z_l} \tag{2.2}$$

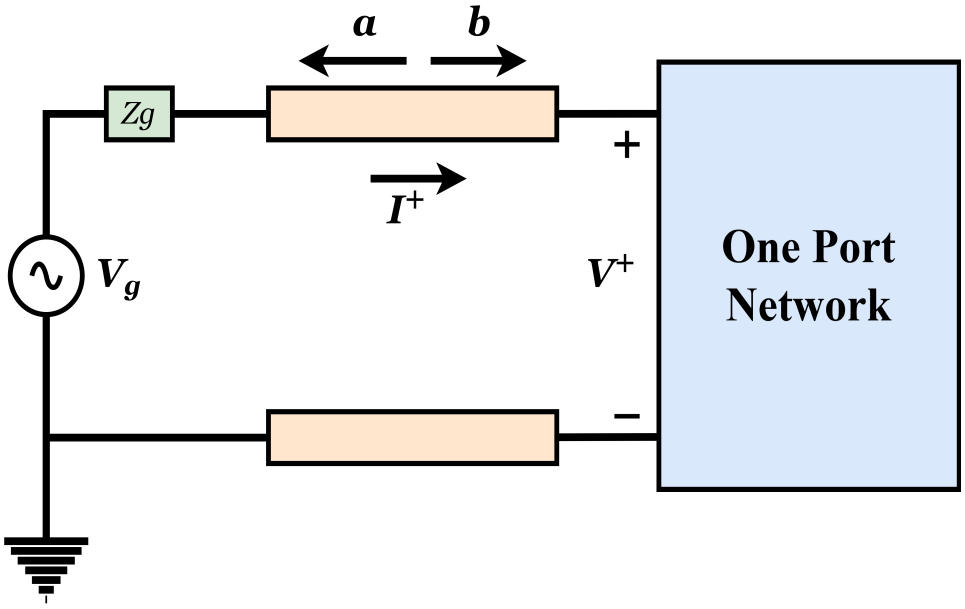

Figure 2.1 One port network connected with generator having Z_g as impedance.

It can be noticed from (2.1), (2.2) that incident current and voltage both are dependent on every parameter i.e Z_g, Z and V_g present in the network.
In order to receive the maximum available power from generator in the load, the load impedance must be euqal to the conjugate of i.e $Z_l = {Z_g}^*$. Let us assume, $Z_g = R_g + jX_g$; then, the incident current and voltage are as follows [30],

$$I^+ = \frac{V_g}{(Z_g + Z_g^*)} = \frac{V_g}{2R_g} \tag{2.3}$$

$$\begin{aligned} V^+ &= Z_g^* \frac{V_g}{(Z_g + Z_g^*)} \\ &= Z_g^* \frac{V_g}{2R_g} \\ &= (R_g + jX_g)\frac{V_g}{2R_g} \end{aligned} \tag{2.4}$$

Therefore,

$$V^+ = R_g \frac{V_g}{2R_g} + jX_g \frac{V_g}{2R_g} \tag{2.5}$$

Furthermore, from figure 1.1 we can say that the relationship between incident voltage and incident current is,

$$V^+ = Z_g^* I^+ \tag{2.6}$$

Also, the maximum power available is,

$$\begin{aligned} P_{avail} &= \frac{1}{2} Re[VI^*] \\ &= \frac{|V_g|^2}{8R_g} \end{aligned} \tag{2.7}$$

It can be noticed from (2.3), (2.5) and (2.7) that incident current, voltage and maximum available power respectively are independent of the impedance of the one-port network.

Furthermore, from law of conservation of energy, this maximum available power, P_{avail} is equal to the maximum power delivered to the load i.e one-port network. As,

$$V = V^+ + V^- \tag{2.8}$$

and,

$$I = I^+ + I^- \tag{2.9}$$

Hence, incident power at one-port network will be,

$$\begin{aligned} P_{inc} &= \frac{1}{2} Re[V^+ (I^+)^*] \\ &= \frac{|V_g|^2}{8R_g} \end{aligned} \tag{2.10}$$

Therefore, after rearranging (2.4) we get,

$$V_g = 2R_g \frac{V^+}{Z_g^*} \tag{2.11}$$

Now, Substituting above (2.11) in (2.10), we get,

$$P_{inc} = \frac{R_g |V^+|^2}{2|Z_g^*|^2} \tag{2.12}$$

Hence, let us assume a and b as normalised incident wave and reflected wave, therefore, the magnitude of a and b is defined as square root of incident and reflected powers respectively, which is as follows,

$$
\begin{aligned}
|a| &= \sqrt{P_{inc}} \\
&= \sqrt{\frac{R_g|V^+|^2}{2|Z_g^*|^2}} \\
&= \frac{V^+}{Z_g^*}\sqrt{\frac{R_g}{2}} \\
&= I^+\sqrt{\frac{R_g}{2}}
\end{aligned}
\tag{2.13}
$$

$$
\begin{aligned}
|b| &= \sqrt{P_r} \\
&= \sqrt{\frac{R_g|V^-|^2}{2|Z_g^*|^2}} \\
&= \frac{V^-}{Z_g^*}\sqrt{\frac{R_g}{2}} \\
&= I^-\sqrt{\frac{R_g}{2}}
\end{aligned}
\tag{2.14}
$$

The ratio of normalised reflected wave and normalised incident wave is known as reflection coefficient. It is generally denoted by Γ. As,

$$
\Gamma = \frac{a}{b} \tag{2.15}
$$

2.1.2 The Scattering Matrix

The Scattering parameters defines the relationship between the voltage at incident wave port with the voltage at reflected or transmitted wave ports. The Scattering matrix characterises a microwave network at specific frequency and operating condition using these scattering parameter. Let us consider a two port network as shown in Figure 1.2 having transmission line characteristic impedance to be $Z_{TL} = Z_0$; then the scattering matrix for a two-port network can be defined as follows,

$$
\begin{bmatrix} b_1 \\ b_2 \end{bmatrix} = \begin{bmatrix} s_{11} & s_{12} \\ s_{21} & s_{22} \end{bmatrix} \begin{bmatrix} a_1 \\ a_2 \end{bmatrix} \tag{2.16}
$$

where, the s_{11} is the input reflection coefficient while the output is terminated with Z_0,

$$
s_{11} = \left.\frac{b_1}{a_1}\right|_{a_2=0} \tag{2.17}
$$

the s_{21} is the forward transmission coefficient between Z_0 terminations,

$$
s_{21} = \left.\frac{b_2}{a_1}\right|_{a_2=0} \tag{2.18}
$$

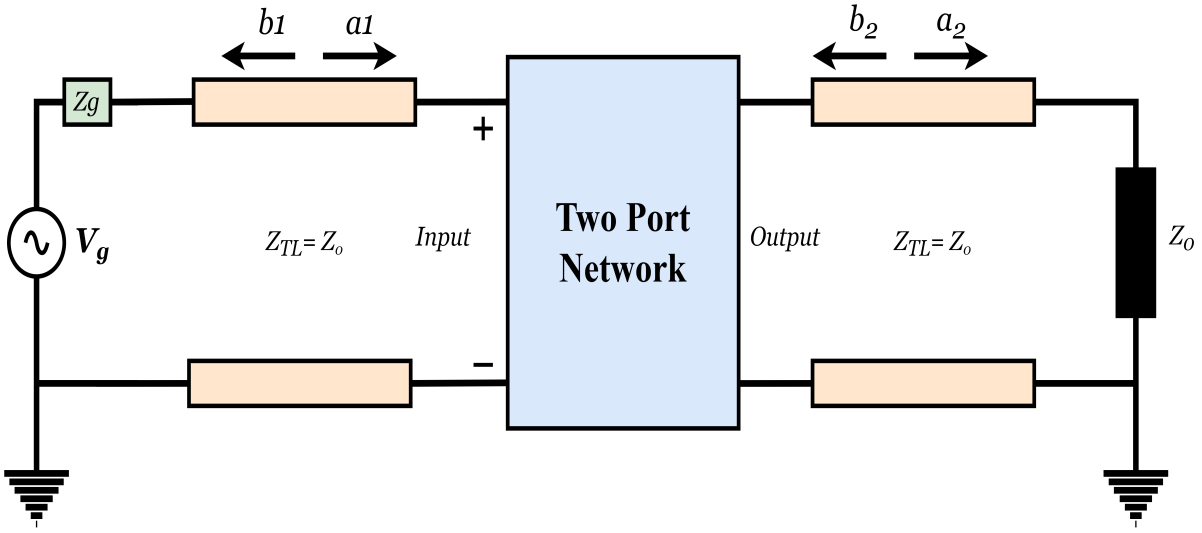

Figure 2.2 Two port network

the s_{12} is the reverse transmission coefficient between Z_0 terminations,

$$s_{12} = \left.\frac{b_1}{a_2}\right|_{a_1=0} \tag{2.19}$$

the s_{22} is the output reflection coefficient while the input is terminated with Z_0,

$$s_{22} = \left.\frac{b_2}{a_2}\right|_{a_1=0} \tag{2.20}$$

In a lossless transmission line two-port network, the total power applied to the input port either get reflected or transmitted completely depending on the load impedance value. Hence, this statement proves the below equation,

$$|s_{11}|^2+|s_{21}|^2 = 1 \tag{2.21}$$

The above equation also satisfy the law of conservation of energy. The scattering parameters can be calculated using some network analysis techniques. Otherwise, Vector Network Analysers (VNAs) are used for finding the scattering parameters.

A vector Network Analyser is a two channel (or four channel) device designed to measure the magnitude and phase of reflected and transmitted waves. Nowadays, VNA process the data and are able to calculate and display the impedance and scattering parameters. The traditional Vector Network Analysers generally consists of three important blocks: 1) Radio Frequency (RF) Synthesizer 2) IF processing and 3) Digital processing. To measure the scattering parameters of a Test Set, RF synthesizer which acts as RF source, sweeps over a specific frequency bandwidth, and for the measurement of magnitude and phase information, the four-port reflectometer samples the incident, reflected and transmitted RF waves. Figure 2.3 shows the basic block diagram of a VNA and Figure 2.4 shows an image of a traditional

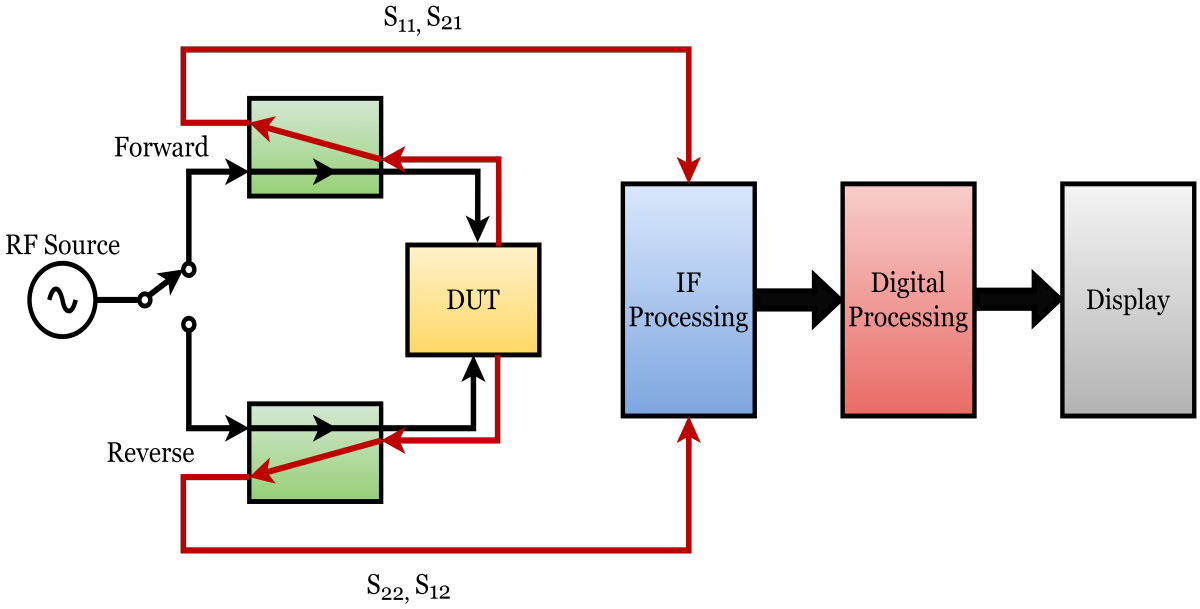

Figure 2.3 Block diagram of Vector Network Analyser

VNA.

2.2 Microwave Circuit Design Technologies

2.2.1 Microwave Transmission Lines

A transmission line is way of propagating power in microwave systems and it basically consists of two or more parallel conductors used to connect a source to a load. Figure 2.5 shows some examples of transmission lines like coaxial cable, a two-wire line, a parallel-plate or planar line, a wire above the conducting plane, and a microstrip line [31]. Notice that each of these lines consists of two conductors in parallel. Transmission lines are also used to design some passive microwave devices like power divider, directional coupler, filters, impedance transformers etc. A transmission line can be characterised by following parameters,

1. Characteristic Impedance, Z_0.
2. Electrical path length, $\theta = \beta l$.

where β is propagation constant and $\beta = 2\pi\sqrt{\varepsilon_{eff}}/\lambda$, l is physical length of transmission line, ε_{eff} is the effective dielectric constant of the line and λ is the free space EM wavelength.

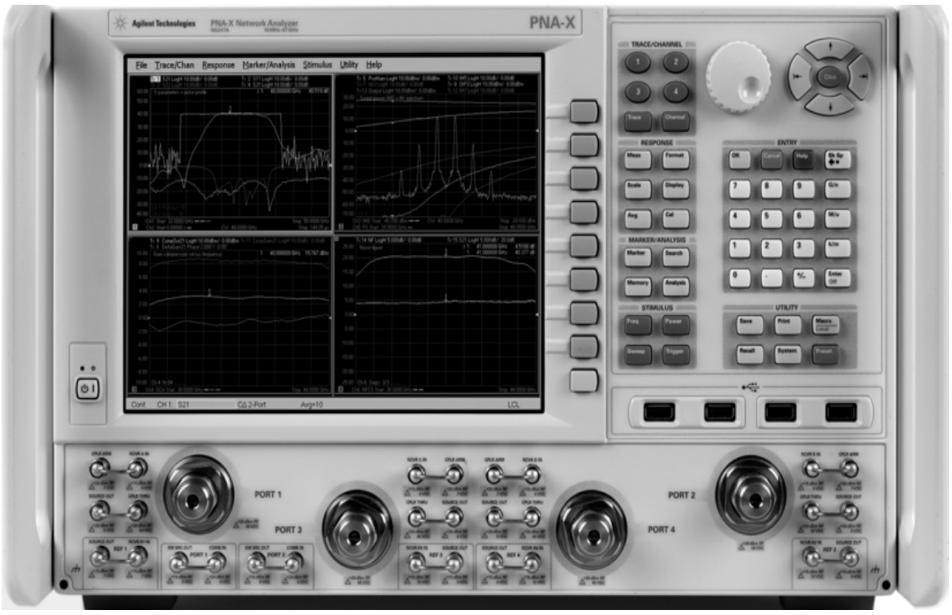

Figure 2.4 Vector Network Analyser [29]

In microwave integrated circuits, the most common transmission line used are microsttrip line, stripline, slot lines, coplaner lines [32], figure 2.6 shows these transmission lines.

Generally, in practical scenarios, a transmission line is terminated with a load, having an impedance of Z_l as shown in the figure 2.7. Let us assume that the transmission line is lossless and the physical length and the characteristic impedance of the transmission line l, Z_0, respectively. Therefore, according to the classic transmission lines theory [29, 31], it can be shown that the input impedance of a lossless terminated transmission line is,

$$Z_{in} = Z_0 \frac{Z_l + jZ_0 \tan(\beta l)}{Z_0 + jZ_l \tan(\beta l)} \tag{2.22}$$

2.2.2 Microwave Passive Circuits

This section presents some of the most common microwave passive circuits that are usually utilised in the microwave systems.
A microwave system consist of active and passive microwave circuits. These passive circuits are the important part for microwave signal processing. Passive circuits are usually realised by utilising microwave transmission lines and lump elements.

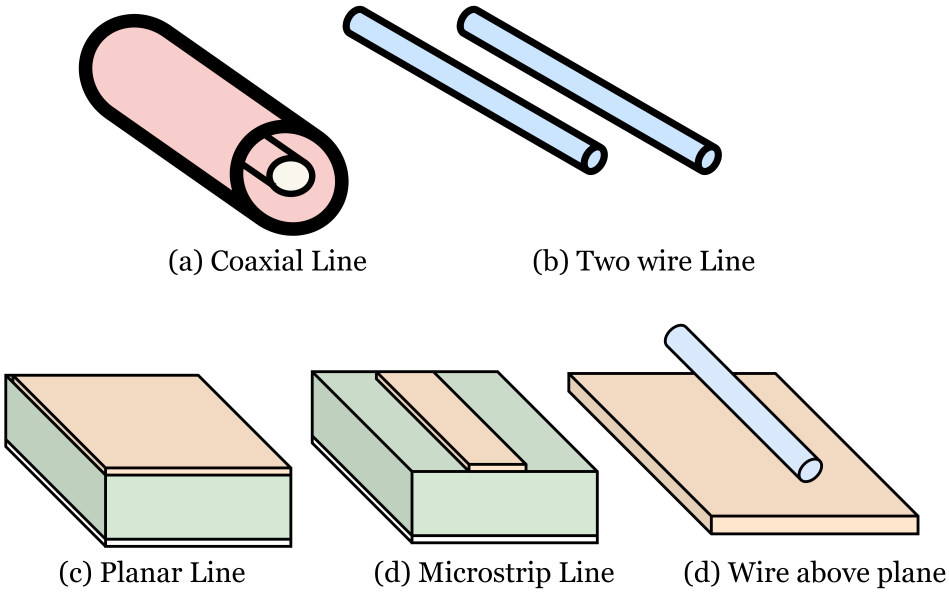

Figure 2.5 Common Transmission lines

2.2.2.1 Wilkinson Power Dividers

The name of this microwave circuits explains its working i.e the power dividers are utilised for splitting the power as illustrated in figure 2.8. It has one input port and 'n' (n ϵ N) output ports depending on the output signals required. Usually, power dividers provide in-phase output signals with an equal power division ratio i.e 3 dB(2-ports), but unequal power division ratios are also possible. There are different kind of power dividers available but in this section we will discuss briefly about Wilkinson Power Dividers. Wilkinson power dividers are often fabricated using microstrip line or stripline. The scattering matrix for an ideal Wilkinson power divider is as follows,

$$\Big[S\Big] = \begin{bmatrix} 0 & -\frac{j}{\sqrt{2}} & -\frac{j}{\sqrt{2}} \\ -\frac{j}{\sqrt{2}} & 0 & 0 \\ -\frac{j}{\sqrt{2}} & 0 & 0 \end{bmatrix} \tag{2.23}$$

2.2.2.2 Directional Coupler

The directional couplers are 4-port microwave passive devices that are utilised to divide power. The critical difference between directional couplers and power dividers is that coupler provides phase shift (usually 90^0 and 180^0) to the divided power whereas power divider does not adds any phase shift. Moreover, a directional coupler is a 4-port device with 1 input and 3-output ports whereas power divider is

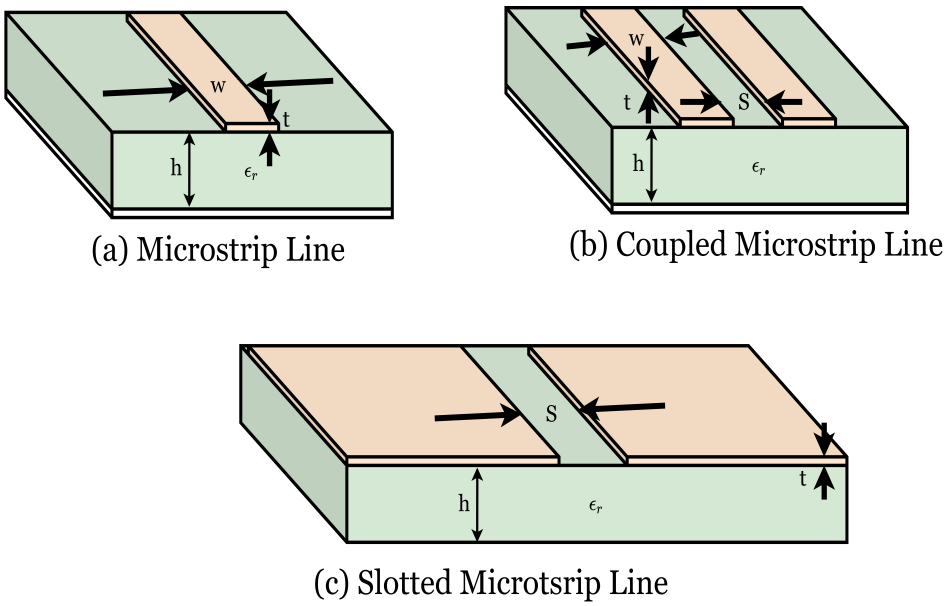

Figure 2.6 Transmission lines used in Intergrated circuits

a 3-port device as described in the previous section. Usually, a directional coupler that is designed for equal power division with 90^0 and 180^0 of phase shifts is known as quadrature hybrid but directional couplers with arbitrary phase shift are possible to design. Mostly, the structure is fabricated over microstrip and stripline. Figure 2.9 illustrates some directional couplers.
The scattering matrix for symmetrical directional coupler is as follows,

$$\Big[S\Big] = \begin{bmatrix} 0 & \alpha & j\beta & 0 \\ \alpha & 0 & 0 & j\beta \\ j\beta & 0 & 0 & \alpha \\ 0 & j\beta & \alpha & 0 \end{bmatrix} \tag{2.24}$$

where, α and β are related as following,

$$\alpha^2 + \beta^2 = 1 \tag{2.25}$$

In an ideal directional coupler, the power coupled to port 3 with coupling coefficient β is known as coupled port, whereas the power transmitted to port 2 with transmitting coefficient α is known as through port and no power is delivered to port 4, hence it is known as isolated port. The following relations are generally used to characterise a directional coupler [29]:

$$\begin{aligned} |s_{13}|^2 &= \beta^2 \\ |s_{12}|^2 &= \alpha = 1 - \beta^2 \end{aligned} \tag{2.26}$$

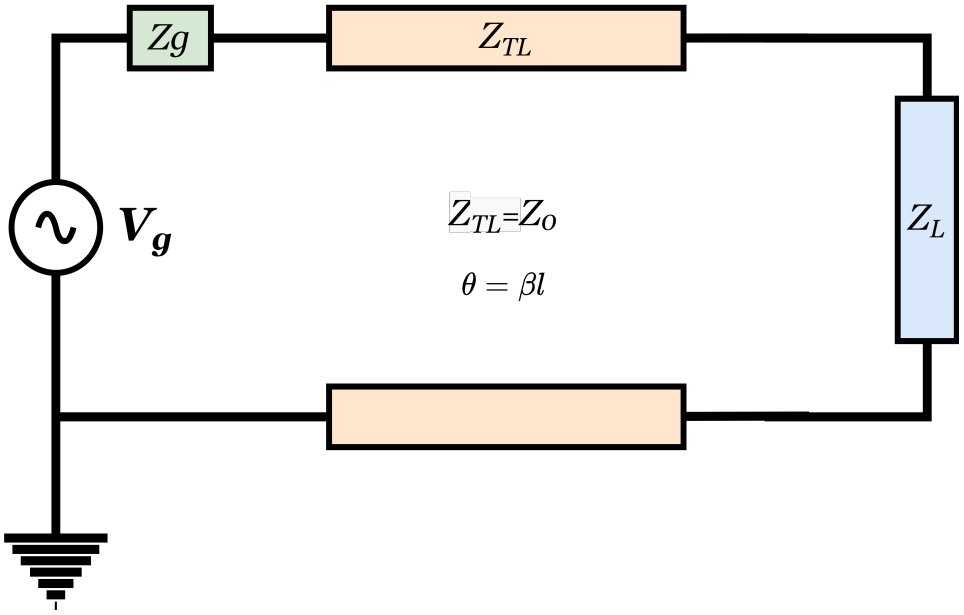

Figure 2.7 A terminated Transmission lines

$$Coupling = C = 10\log\frac{P_1}{P_3} = -20\log\beta \tag{2.27}$$

$$Directivity = D = 10\log\frac{P_3}{P_4} = 20\log\frac{\beta}{|s_{14}|} \tag{2.28}$$

$$Isolation = I = 10\log\frac{P_1}{P_4} = -20\log|s_{14}| \tag{2.29}$$

Quadrature Hybrid Couplers: There couplers are special cases of direction couplers, where the coupling factor is 3 dB and it has a 90 degree phase shift between ports 2 and 3 when fed at port 1 . A hybrid coupler is shown in Figure 2.9. The scattering matrix for the coupler is as follows,

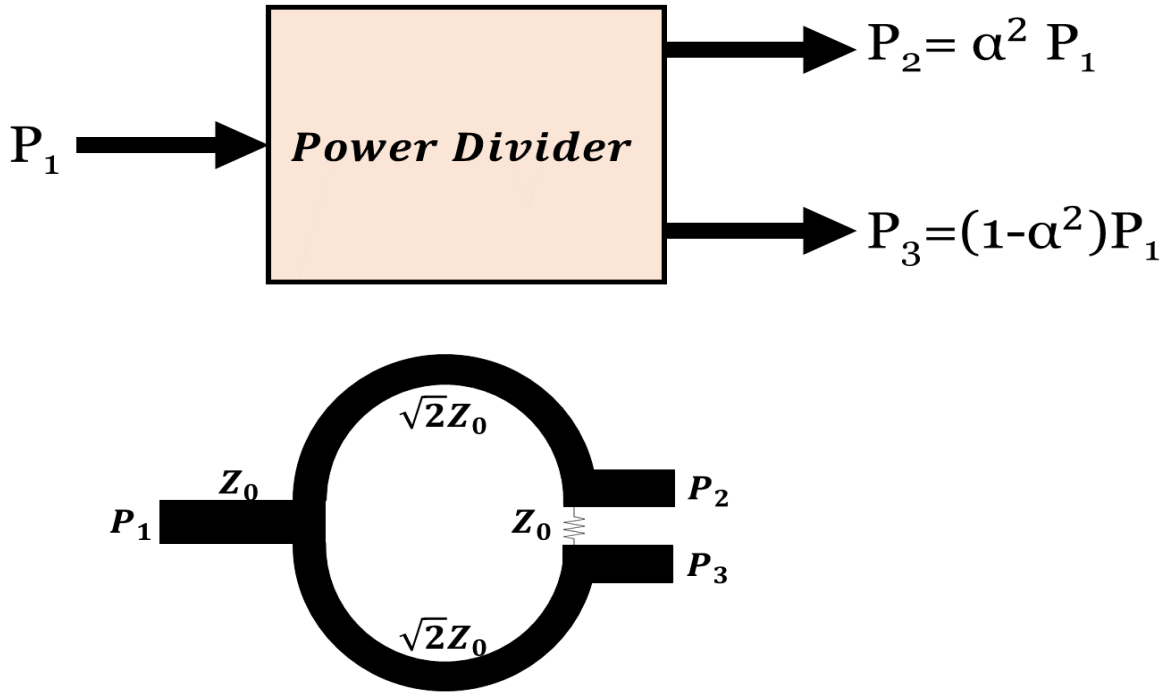

Figure 2.8 A conventional wilkinson power divider with functional block diagram

$$\left[S\right] = \frac{1}{\sqrt{2}} \begin{bmatrix} 0 & 1 & j & 0 \\ 1 & 0 & 0 & j \\ j & 0 & 0 & 1 \\ 0 & j & 1 & 0 \end{bmatrix} \tag{2.30}$$

Rat-Race Couplers: As shown in Figure 2.9, a rat race coupler has a 180 degree phase difference between port 2 and 3 when fed at port 4. The scattering matrix is,

$$\left[S\right] = \frac{1}{\sqrt{2}} \begin{bmatrix} 0 & 1 & 1 & 0 \\ 1 & 0 & 0 & -1 \\ 1 & 0 & 0 & 1 \\ 0 & -1 & 1 & 0 \end{bmatrix} \tag{2.31}$$

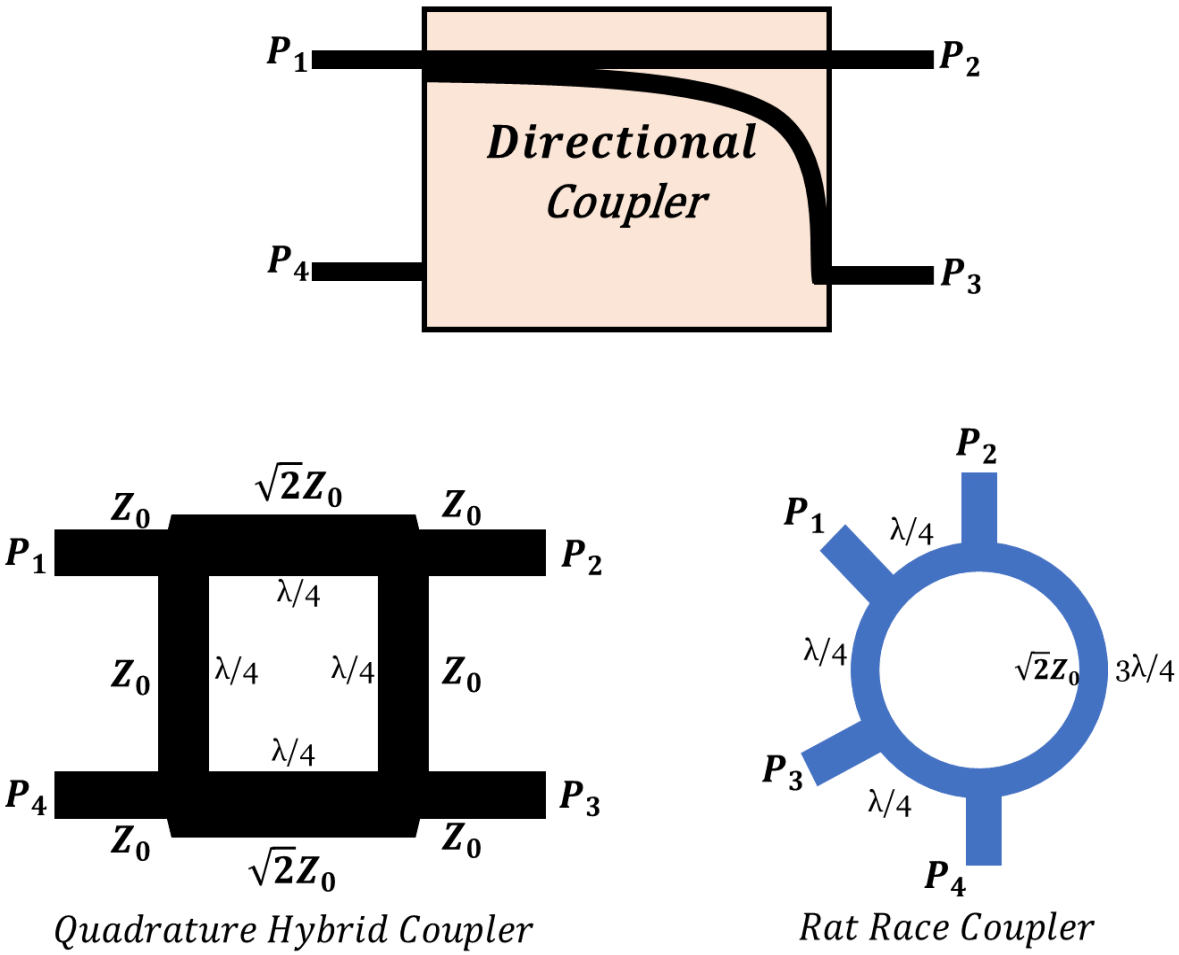

Figure 2.9 Examples of some directional coupler

The microwave passive circuits include power dividers, directional couplers, impedance transformers, filters and resonator. Some of the uses of the devices is shown in Table 2.1,

2.2.3 Fabrication Technologies

The microwave systems can be fabricated using different types fabrication technologies. These fabrication technologies include MIC (Microwave Integrated Circuits), MHMIC (Monolithic Hybrid Microwave Integrated Circuits) and MMIC (Monolithic Microwave Integrated Circuits).
There are two types of microwave devices:

Application vs Device	Matching Circuits	Signal Filtering	Signal Dividing/ Combining	Device Biasing	Impedance Transformer	Phase Transformer
Transmission Lines	High	High	High	High	High	High
Coupled Lines	Low	Moderate	High	Low	Low	High
Lumped Elements	Yes (Low freq.)	Moderate (Low freq.)	Low	High	Low	No
Hybrid Couplers	No	Low	High	No	Low	Yes
Discontinuities	High	High	Low	Yes	Low	No
Resonators	Moderate	High	No	No	No	No

Table 2.1 Microwave Passive Devices and there applications

1. Active Devices : The active devices include diodes like Shottkey, Gunn and Varactor diode and transistors like Bi-polar Junction Transistors (BJT), Field Effect Transistors (FET), Metal-Semiconductor Field Effect Transistors (MESFET), Heterojunction Bipolar Transistor (HBT), and High Electron Mobility Transistors (HEMT).

2. Passive Devices : The passive devices includes Power Dividers, Couplers, Impedance Transformers and Phase Shifters.

In MIC fabrication technology, the active microwave solid state devices and passive devices are mounted together over a dielectric substrate. The device are connected together using passive transmission lines on the same substrate. Generally, this technology is used for the circuits having operating frequency less than 20GHz. The substrate is generally selected with dielectric boards like RT-Duroid having low loss. This circuits are usually larger in size when compared with MHMIC and MMIC with low cost.

Similarly, in MHMIC, usually a substrate having low loss and high dielectric (about 10) is utilised. Both chip devices and circuits are used in this technology. The matching circuits are designed by either distributed or lumped circuits. Furthermore, the circuit size is small and cost is moderate. The circuits having operating frequency upto 50 GHz can be fabricated using MHMIC.

The utilisation of silicon, GaAs, or SiGe makes MMIC technology a better choice for very small circuits. The technology can be efficiently used to fabricated circuits having operating frequency upto

100 GHz. In this circuits, the active devices are fabricated and passive devices are printed over the substrate and the matching circuits are designed using distributed and lumped circuits. The cost for this technology is higher when compared with MHMIC and MIC.

Chapter 3

Design Process of a Dual Band Branch Line Coupler

This chapter presents designing process and simulation results of the proposed dual band branch line coupler. Closed-form design equations are reported for the proposed dual band branch line coupler in subsequent sections.

3.1 Introduction

A Branch-Line Coupler (BLC) is a four-port high-frequency device used for power combining/splitting. They are widely used in balanced amplifiers, mixers, beam-forming networks, and antenna arrays, for example [33], [34].

The most common method for designing a dual-band BLC is to simply replace all of a single-band BLC's quarter-wave lines with equivalent dual-band quarter wave blocks. Dual-band quarter wave blocks include the composite right-/left-hand transmission lines (TLs) [35], Pi-network [36], [37], T-network [38], recently reported modified T-network incorporating coupled line [39], and stepped impedance with open/short stub lines [40], [41]. These reported designs either have a limited band ratio or a complex design procedure, or they provide only equal power division. A few changes to the Pi-network-based dual-band BLCs have also been reported, for example, in [42] to achieve tunability around the two frequencies, in [43] to generalise the same, and, most recently, in [44] to achieve arbitrary phase as well as arbitrary power division.

Another approach was proposed in [45] for designing a coupled line-based branch line coupler, and further improvements were reported to achieve unequal power division [46], [47]. Recently, some dual-band coupler design techniques based on the impedance matching concept [48], [49] have employed the dual-band equivalent of port extension techniques [50], [51]. However, larger board sizes are frequently required in this technique, particularly when cascading to achieve a wider bandwidth.

Traditionally, when a dual-band BLC is obtained by incorporating a T-/Pi-network, it is the single-band BLC of equal length that is at the core, necessitating the replacement of all four arms [52].

3.2 The Proposed Dual Band Branch Line Coupler Design

The proposed structure is a symmetrical design and it consists of four port as shown in the fig. 3.1. The coupler is capable of providing a phase shift of 90° and arbitrary power division. However, for this work an equal power division (3dB) coupler has been designed. The proposed designed has conventional Branch Line Coupler at its core and external matching transmission lines were used for designing a dual band coupler.

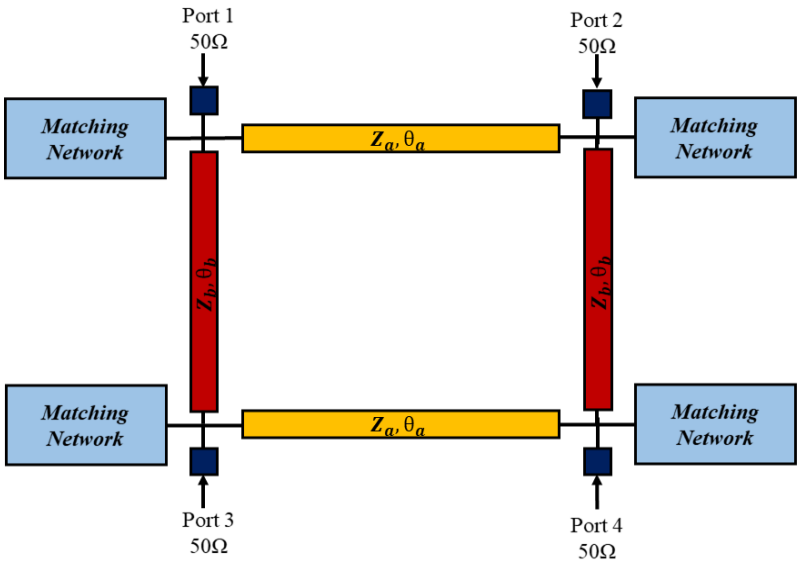

Figure 3.1 Block diagram of proposed dual band branch line coupler

3.3 Design Analysis

3.3.1 Review of a Single Band Branch Line Coupler

Since a dual band coupler has a single Band coupler at its core, therefore, it is important to know and understand the design process of a single band coupler. Figure 3.2 depicts a Branch line coupler with Z_a

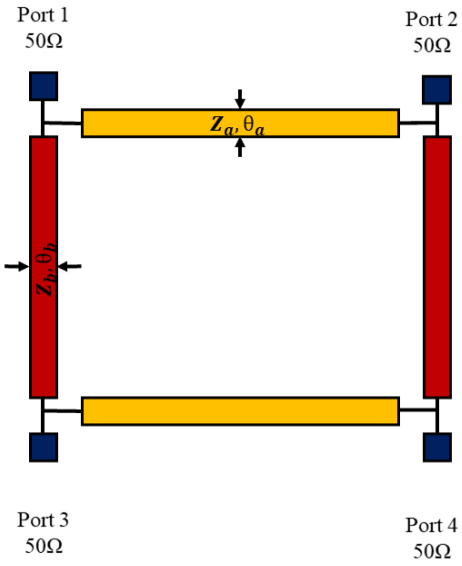

Figure 3.2 Block diagram of a traditional single band branch line coupler

and θ_a as the characteristic impedance and electrical length of the horizontal Transmission line sections, respectively. Whereas, Z_b and θ_b are the corresponding terms for vertical TL sections. According to fig. 3.2 following are the port description of the coupler:

1. Port 1 : Input port
2. Port 2 : Through port
3. Port 3 : Coupled port
4. Port 4 : Isolated port

Let us assume α is power division ratio of the coupler, such that,

$$P_2 = \alpha^2 P_1 \tag{3.1}$$

where, $\alpha^2 \epsilon$ (0,1) and, P_1 and P_2 are power at port 1 which is input power and power through output port 2 respectively. The required conditions and equations for designing of Single band Branch line coupler are discussed in [53]. Therefore, the parameters for coupler can be expressed as follows,

$$Z_a = \frac{\alpha Z_0}{\sqrt{\alpha^2 + (1-\alpha^2)\sin^2\theta_b}} \tag{3.2}$$

$$Z_b = \frac{\alpha Z_0}{\sqrt{1-\alpha^2}|\sin\theta_b|} \tag{3.3}$$

$$\tan\theta_a = -\frac{Z_b}{Z_a}\tan\theta_b \tag{3.4}$$

where, Z_0 is the characteristic impedance of the transmission line. Also, using equation 3.4,3.2 and 3.3 can be written in terms of θ_a as follows,

$$Z_a = \frac{\alpha Z_0}{|\sin\theta_a|} \tag{3.5}$$

$$Z_b = \frac{\alpha Z_0}{\sqrt{\sin^2\theta_a - \alpha^2}} \tag{3.6}$$

The next section presents the design analysis of dual band branch line coupler using pi-stub technique.

3.3.2 Dual Band Branch Line Coupler

As discussed earlier, a single band coupler is utilised and modified for designing a dual band coupler. To understand this concept, we can consider equation 3.2 and 3.3 of single band coupler. These equations consist of sinusoidal function. In a sinusoidal function, suppose the value of the function at θ is K then the same value will repeat itself at $\pi - \theta$. Therefore, as we knew in a transmission line electrical length is directly proportional to the operating frequency. Hence, if at a operating frequency of f_1 the electrical length is θ with Z as value of impedance then to get the same impedance value at f_2, it must be K times ratio of two electrical lengths. This can be understood by the fig. 3.3 and following equations:

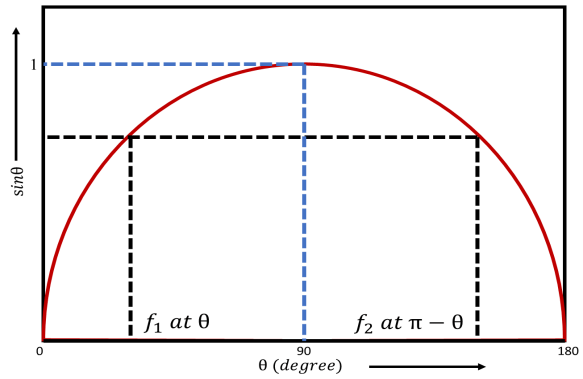

Figure 3.3 Sinusoidal Function

$$\theta_b = f_1 \tag{3.7}$$

$$\pi - \theta_b = f_2 \tag{3.8}$$

Hence, from equation 3.7 and 3.8 θ_b can be written as follows,

$$\theta_b = \frac{\pi}{(1+r)} \tag{3.9}$$

where, $r = f_2/f_1$ is the frequency band ratio and $r > 1$.

The proposed dual band branch line coupler has been designed using a pi-stub technique as shown in figure 3.1. The dual band nature of the branch line coupler is obtained by replacing the vertical transmission lines of a conventional branch line coupler with a Pi Stub network. This Pi stub network consist of a verticle transmission line with Z_s, θ_s as characterstic impedance and electrical lenght. It also consist of two side stubs with admittance of jB_s connected to the both ends of the vertical transmission line as shown in the figure 3.4.

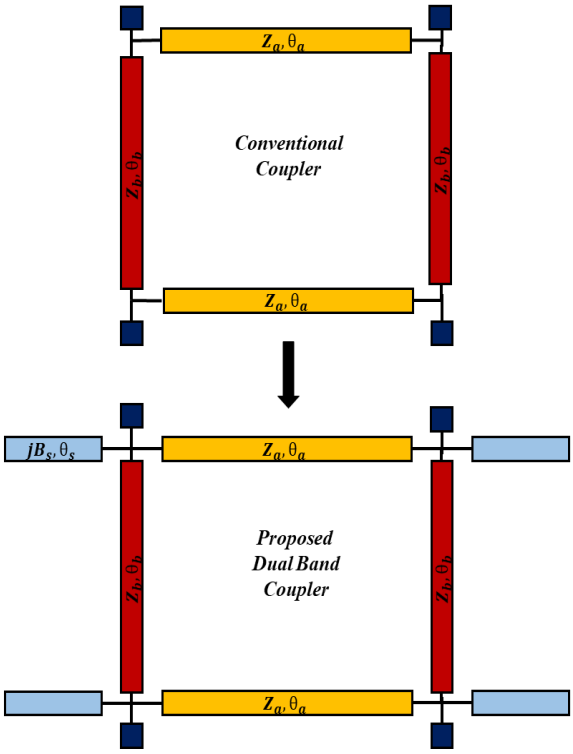

Figure 3.4 Conventional to Dual Band Coupler using Pi-Stub Technique

Following design equations were obtained from [54],

$$Z_s = \frac{Z_a}{\sqrt{(1-\alpha^2)}} = \frac{\alpha Z_0}{\sqrt{(1-\alpha^2)}|\sin\theta_a|} \tag{3.10}$$

$$B_s = \frac{1 + \frac{1}{\sqrt{(1-\alpha^2)}}}{Z_s} \cot\theta_s = (\frac{1}{Z_s} + \frac{1}{Z_a}) \cot\theta_a \tag{3.11}$$

where, $\theta_s = \theta_a$. Hence, by using these equations and by choosing a suitable $\alpha > 1$, the impedance and electrical length for the dual band branch line coupler can be calculated. The subsequent section presents the simulated results of the designed dual band branch line coupler.

3.4 Design Parameters and Simulation Results

Transmission lines vs Dimensions	**Length (in mm)**	**Width (in mm)**
Vertical Transmission Lines	32	0.985
Horizontal Transmission Lines	26	4.689
Open Circuited Stub	32	0.667

Table 3.1 Design parameters for dual band coupler.

3.4.1 Design Parameters

Following the design theory and analysis done in the previous section, a dual band branch line coupler was designed and simulated in NI AWR Microwave office (AXIEM). The proposed coupler was designed over RT-duroid 5880 as substrate. The required parameters for the RT Duroid 5880 are as follows :

1. height, $h_s = 1.6mm$
2. dielectric constant, $\epsilon_r = 2.2$,
3. tangent loss, $\tan\delta = 0.0037$,
4. top copper layer thickness, $T_{top} = 35\mu m$,
5. bottom copper layer thickness, $T_{bottom} = 35\mu m$.

Fig. 3.7 and fig. 3.8 displays the schematic and layout of proposed dual band coupler in AWR respectively. Table 3.1 shows all the required parameter utilised to design the dual band coupler.

3.4.2 Simulation Results

All the simulation of proposed design are carried out in CADENCE AWR Microwave (AXIEM). Electro-Magnetic (EM) simulation results for various scattering parameters are plotted and analyzed in details. The return loss (S_{11} parameter) are shown in Fig. 3.5. From Fig. 3.5 it is clear that the return loss at the two operating frequencies is less than -20 dB for EM simulation. Insertion loss (S_{21} parameter) is shown in fig. 3.5 also known as transmission parameter has a value less than 3 dB at all two operating frequencies which shows a good transmission of power is happening. Moreover, from fig. 3.6 it can be note that Isolation coefficient (S_{41}) of less -20 dB has been obtained the operating frequencies which shows very negligible power is reaching to port 4. Furthermore, on -7 dB and -6 dB of S_{31} i.e coupling coefficient is achieved which shows a huge amount of power is getting coupled to port 3. The above results shows that the designed coupler is working at the desired designed operating frequencies.

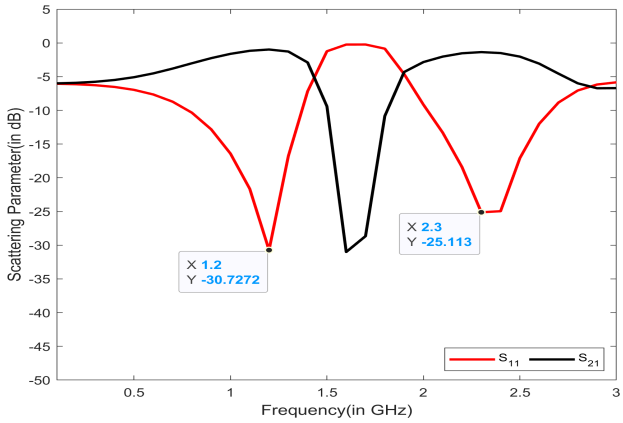

Figure 3.5 S_{11} and S_{21} parameters of the dual band coupler.

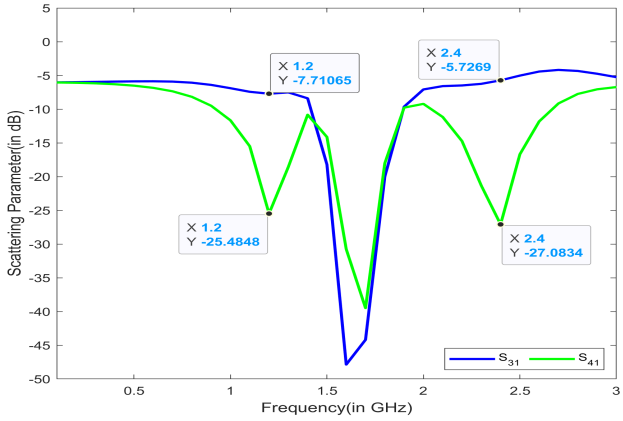

Figure 3.6 S_{31} and S_{41} parameters of the dual band coupler.

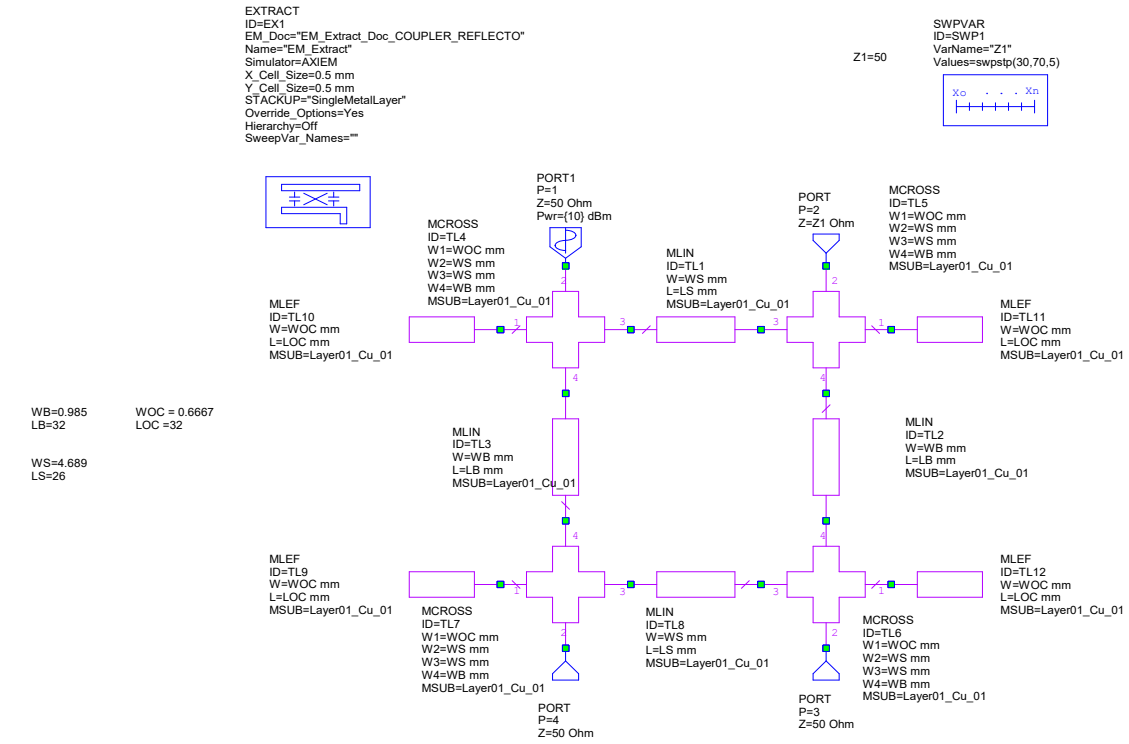

Figure 3.7 Schematic of proposed dual band coupler using Pi-stub technique in AWR.

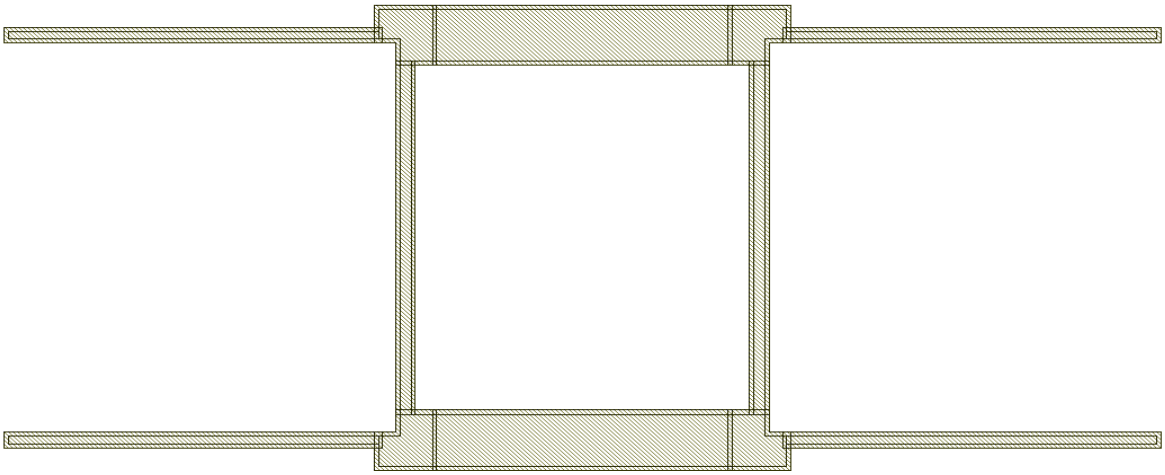

Figure 3.8 Layout of proposed dual band coupler using Pi-stub technique in AWR.

Chapter 4

Design and Simulation of Dual Band Wilkinson Power-Divider

This chapter discusses about the designing methods and topology used for designing a dual band Wilkinson Power Divider. Moreover, it also discusses about the closed form equations used in designing and simulation results in the subsequent sections.

4.1 Literature Review

In microwave systems, Power dividers are an inevitable component. They can divide a single input signal into two or more output signals, or they can combine two or more signals into a single signal. Antenna phase arrays, mixers, I/Q modulators, and demodulators are all examples of devices that use this function. However, there are some limitation like limited bandwitdh, large area occupancy and single band operation. These limitations have been tried to overcome in past by improving size compactness in [55], wide isolation [56] and multiple passways [57].

Moreover, various research articles [58–65]have proposed variety of multi-band power dividers for multi-band microwave applications. In traditional ways, multiple open-/closed-stubs are used with the conventional structure to provide the multi-band function in power divider as described above. However, due to the addition of these stubs the designing process gets more complex and the size becomes bulkier. This increase in size issue was addressed by utilising coupled lines in [63], [64]. However, it simultaneously increases the complexity and it is difficult to achieve equal power division at the two ports.

Furthermore, there are still some research studies [65], [66] which are realising multi-band power dividers using multi-section transmission lines and an isolation resistor.

4.2 Design Theory

4.2.1 Dual Band Wilkinson Power Divider

This subsection provides design methodology involved and closed form equations required for designing power divider. Theoretical analysis is performed to demonstrate the mechanism of dual band operation.

The structure of the dual-band Wilkinson Power divider is shown in Fig. 4.1, where the input port is extended using the microstrip line Z_1, and multi -section stepped impedance transmission lines, composed of Z_2 and Z_3, are used to replace the conventional quarter-wavelength impedance transformer. To reduce design complexity, all transmission lines electrical lengths are assumed to be θ_T. Because of the high symmetry of the structure across horizontal line, even- and odd-mode circuits are used to analyse the mechanism of the power divider and derive the exact design equations. Fig 4.2 displays the even and odd mode circuits utilised for theoretical analysis.

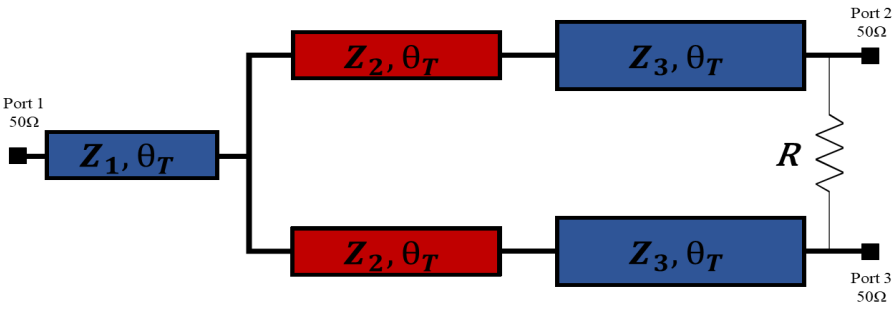

Figure 4.1 Dual Band Wilkinson Power Divider using multi-section Technique

4.2.1.1 Odd-Mode Circuit Analysis

An odd mode circuit of Power divider has been shown in fig. 4.2(a). Since, the analysis is odd mode, therefore the input port and the common input transmission line Z_1 have been shorted and removed. Moreover, the value of isolation resistor has been reduced to its half. It can be observed that in fig. 4.2(a) Z_{IN0}, Z_{IN1} and Z_{INODD} are the impedance looking from the output side of transmission

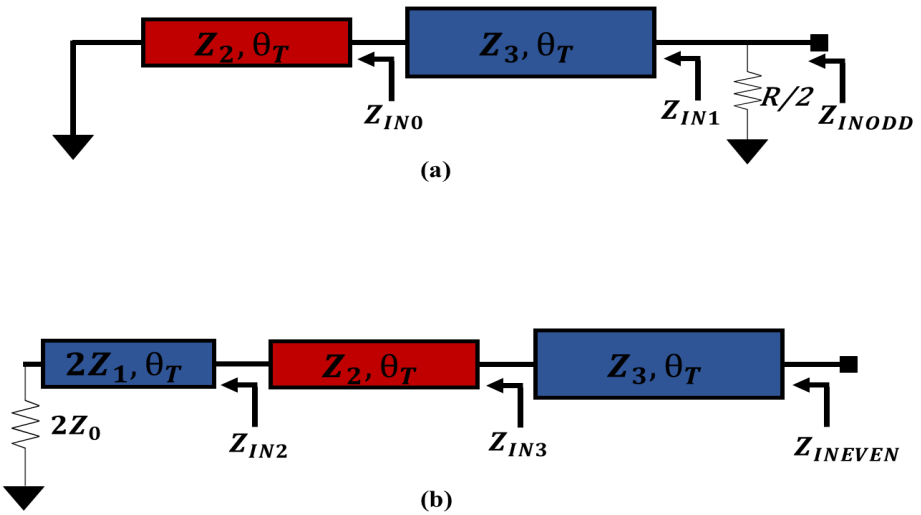

Figure 4.2 Even and Odd Mode circuits for dual band wilkinson power divider.

line Z_2, Z_3 and from the output port respectively, towards the input side of the circuit. Conventional Impedance transformation theory of transmission line can be applied to get the following equations:

$$Z_{IN0} = jZ_2 \tan\theta_T \tag{4.1}$$

$$Z_{IN1} = Z_3 \frac{Z_{IN0} + jZ_3 \tan\theta_T}{Z_3 + jZ_{IN0} \tan\theta_T} \tag{4.2}$$

$$Z_{INODD} = Z_{IN1} || \frac{R}{2} \tag{4.3}$$

The above equation can also be combined and written as following,

$$Z_{INODD} = \frac{Z_3 R(jZ_2 \tan\theta_T + jZ_3 \tan\theta_T)}{R(Z_3 + j(jZ_2 \tan\theta_T)\tan\theta_T) + 2Z_3(jZ_2 \tan\theta_T + jZ_3 \tan\theta_T)} \tag{4.4}$$

For power divider to be working the impedance Z_{INODD} must satisfy following condition,

$$Z_{INODD} = Z_0 = 1 \tag{4.5}$$

After further calculations by using equation 4.5 in equation 4.4 and after rearranging real and imaginary parts, following equations were obtained,

$$Z_3 = Z_2 \tan^2 \theta_T \tag{4.6}$$

$$R = 2 \tag{4.7}$$

It is important to mention here that all the transmission line impedances were normalised to Z_0.

4.2.1.2 Even Mode Circuit Analysis

In even mode analysis, a virtual open circuited plane is placed at the symmetrical position i.e horizontal plane as shown in fig. 4.2(b). As the circuit is open circuited therefore isolation resistor R will have no influence and input port and common line impedance will be $2Z_0$ and $2Z_1$. Moreover, Z_{IN2}, Z_{IN3} and Z_{INEVEN} are the equivalent impedances seen from the ends of transmission lines Z_1, Z_2 and Z_3 towards the input port. After applying basic transmission line impedance transformation theory to the circuit, the following equations can be obtained,

$$Z_{IN2} = 2Z_1 \frac{2 + j2Z_1 \tan \theta_T}{2Z_2 + j2 \tan \theta_T} \tag{4.8}$$

$$Z_{IN3} = Z_2 \frac{Z_{IN2} + jZ_2 \tan \theta_T}{Z_2 + jZ_{IN2} \tan \theta_T} \tag{4.9}$$

$$Z_{INEVEN} = Z_3 \frac{Z_{IN3} + jZ_3 \tan \theta_T}{Z_3 + jZ_{IN3} \tan \theta_T} \tag{4.10}$$

Therefore, for power divider to work in even mode, the resultant impedance Z_{INEVEN} must follows below condition,

$$Z_{INEVEN} = Z_0 = 1 \tag{4.11}$$

Also, the above analysis and following equations were mention in detailed in [67]. Moreover, after solving equation 4.8, 4.9, 4.10 and 4.11, and rearranging real and imaginary parts, the relationship between

θ_T, Z_1, Z_2 and Z_3 can be expressed as follows,

$$\frac{\tan^2\theta_T(1+\tan^2\theta_T)Z_2^2}{2+2\tan^2\theta_T Z_1^2} = 1 \tag{4.12}$$

$$2(-1+\tan^2\theta_T)Z_1 + 2\tan^2\theta_T(-1+\tan^2\theta_T)Z_1^3 - \tan^2\theta_T Z_1^2 Z_2 + \tan^2\theta_T Z_2 = 0 \tag{4.13}$$

It can be observed that most of the equations of all the impedances Z_1, Z_2 and Z_3 for even and odd mode analysis were dependent on $\tan\theta_T$. Hence, to meet the dual band brand conditions θ_T must meet the following conditions,

$$\theta(f_1) = n\pi - \theta(f_2) \tag{4.14}$$

where, n is an arbitrary number, f_1 and f_2 are lower and upper band frequencies and θ is electrical length of the transmission line. Also, according to transmission line theory as electrical length is directly proportional to operating frequency, hence the following relationship holds,

$$\frac{\theta(f_1)}{\theta(f_2)} = \frac{f_1}{f_2} \tag{4.15}$$

Now solving equation 4.14 and 4.15, where frequency ratio, $k = f_2/f_1$ we get,

$$\theta(f_1) = \frac{n\pi}{1+k} \tag{4.16}$$

$$\theta(f_2) = \frac{kn\pi}{1+k} \tag{4.17}$$

Here, it must be noted that the more the value on n the more bigger will be the device. Therefore, two keep the size small, n=1 has been selected for designing power divider. Next subsequent section include simulation results and layout diagram of dual band power divider.

4.3 Design Parameters, layout and Simulation Results

4.3.1 Design Parameters

Following the design theory and analysis done in the previous section, a dual band power divider was designed and simulated in NI AWR Microwave office (AXIEM). The proposed coupler was designed over RT-duroid 5880 as substrate. The required parameters for the RT Duroid 5880 are as follows :

1. height, $h_s = 1.6mm$
2. dielectric constant, $\epsilon_r = 2.2$,
3. tangent loss, $\tan\delta = 0.0037$,
4. top copper layer thickness, $T_{top} = 35\mu m$,
5. bottom copper layer thickness, $T_{bottom} = 35\mu m$.

Fig. 4.4 and fig. 4.5 displays the schematic and layout of proposed dual band coupler in AWR respectively. Table 4.1 shows all the required parameter utilised to design the dual band coupler.

Transmission lines vs Dimensions	**Length (in mm)**	**Width (in mm)**
Input Side Transmission Lines	5	5
Middle Transmission Lines	12.5	1.58
Output side Transmission Lines	12.7	2.85

Table 4.1 Design parameters for dual band power divider.

4.3.2 Simulation Results

The simulation of proposed dual band power divider are carried out in CADENCE AWR Microwave (AXIEM). Electro-Magnetic (EM) simulation results for various scattering parameters were plotted and analyzed. The return loss (S_{11} parameter) in Fig. 4.3 shows that its magnitude at the two operating frequencies is less than -20 dB. Also, Insertion loss (S_{21}/S_{31} parameter) is shown in fig. 4.3 also known as transmission parameter has a magnitude approximately equal to 3 dB at all two operating frequencies which shows a good and equal split of power is happening at the two output ports. Moreover, from fig. 4.3 it can be note that Isolation coefficient (S_{32}/S_{23}) of less than -20 dB has been obtained at the operating frequencies which shows very negligible power is reaching to port 3 to port 2. The above

results proves that the designed dual band power divider is working at the desired designed operating frequencies.

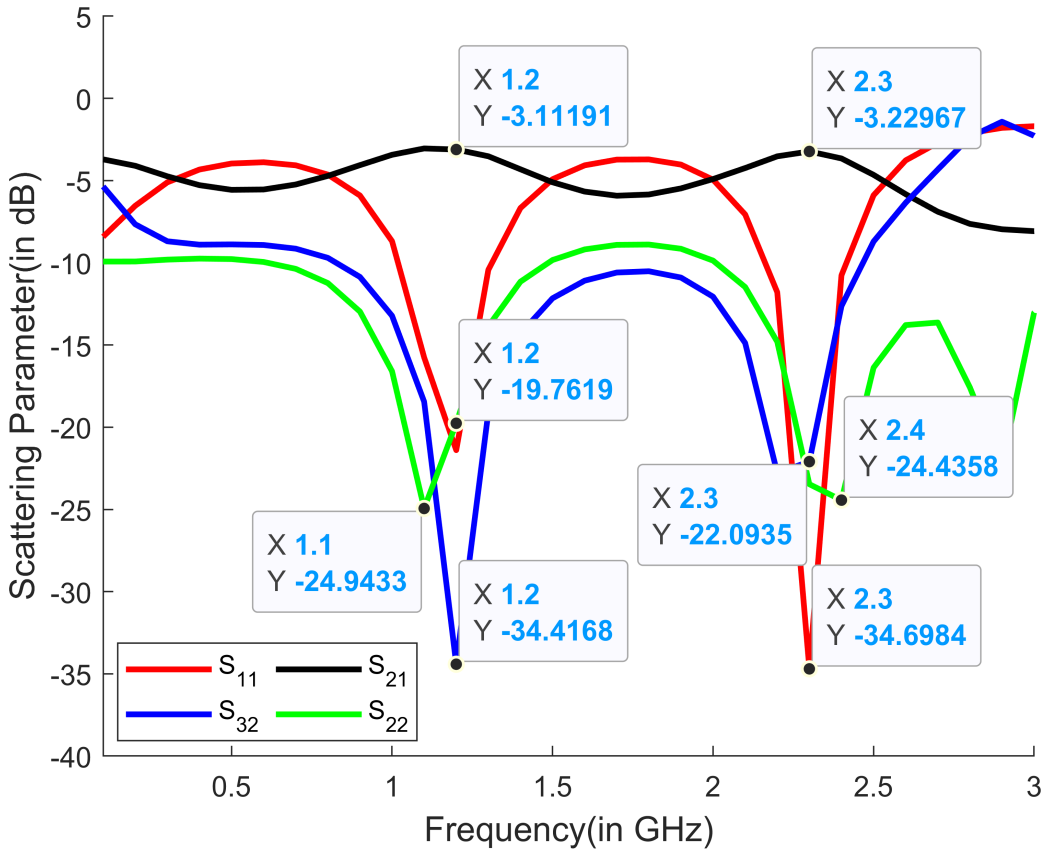

Figure 4.3 S-parameters of the dual band wilkinson power divider.

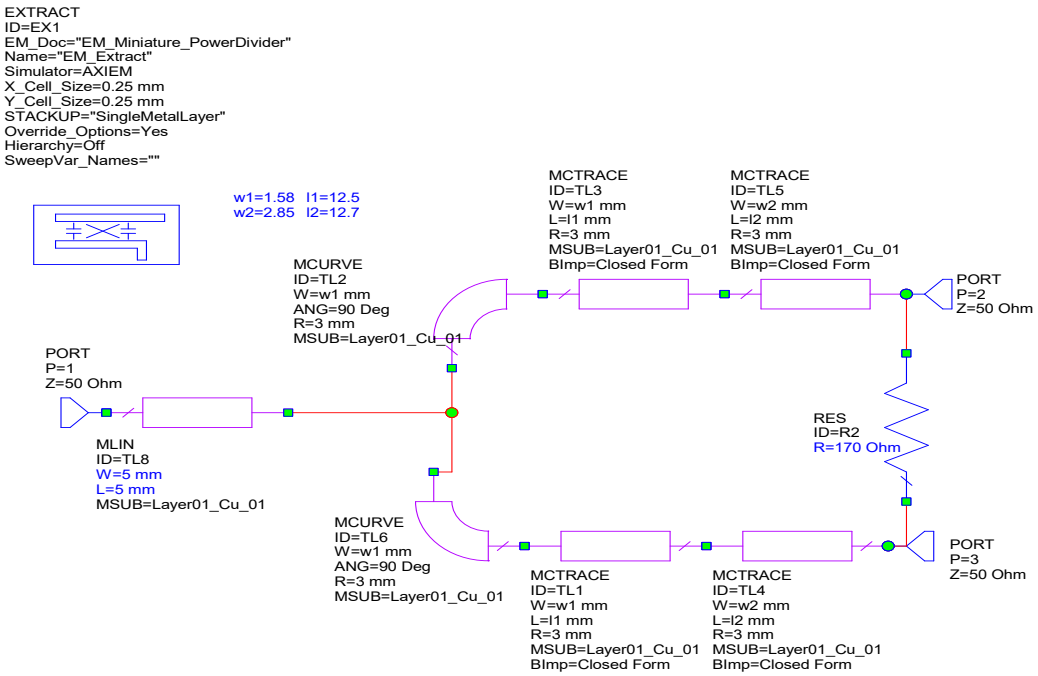

Figure 4.4 Schematic of proposed dual band coupler using Pi-stub technique in AWR.

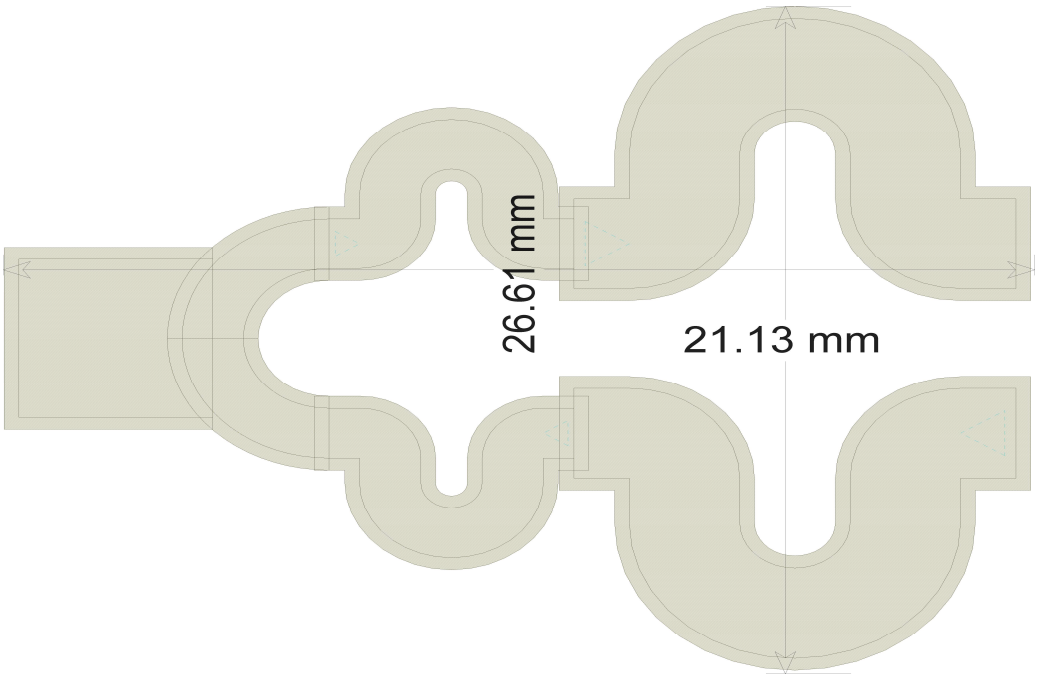

Figure 4.5 Layout of proposed dual band coupler using Pi-stub technique in AWR.

Chapter 5

Design, Simulation and Experimental Results of Dual Band Integrated Bio-sensing Network Analyser

This chapter presents designing process of dual band Six port reflectometer and proposed dual band Integrated Bio-sensing Network Analyser (IBNA). Moreover, the subsequent sections will present the simulation and experimental results performed by using glucose and sucrose as Material Under Test (MUT) with different RF Bio liquid cavities based on Complimentary Split Ring Resonantor (CSRR) and Inter Digitated Capacitor (IDC).

5.1 The Basic Idea behind Six Port Reflectometer

Consider two sinusoidal voltage signals $a_1 and a_2$ having same frequency and phase angle of ϕ between them as shown in Fig. 5.1 (a). Therefore, the sum and difference of those two signals can be written as follows:

$$|a_1 + a_2|^2 = |a_1|^2 + |a_2|^2 + 2|a_1 a_2| \cos\phi \tag{5.1}$$

$$|a_1 - a_2|^2 = |a_1|^2 + |a_2|^2 - 2|a_1 a_2| \cos\phi \tag{5.2}$$

adding above two equations gives us the below equation:

$$\begin{aligned} |a_1 + a_2|^2 + |a_1 - a_2|^2 &= 4|a_1 a_2| \cos\phi \\ \cos\phi &= \frac{|a_1 + a_2|^2 + |a_1 - a_2|^2}{4|a_1 a_2|} \end{aligned} \tag{5.3}$$

The disadvantage of calculating phase angle ϕ from the above equations is that $\cos\phi$ is sensitive to angles near 90° and 270° but insensitive to angles near 0° and 180°.Hence, in addition to $\cos\phi$, $\sin\phi$ is needed, which is sensitive to angles near 0° and 180° and which also gives the sign of the phase angle. Therefore, to get $\sin\phi$, the signals needs to be shifted by 90° and then addition and subs traction needs

to be done as shown in Fig. 5.1 (b). The sum and difference are shown in below equations :

$$|a_1 + ja_2|^2 = |a_1|^2 + |a_2|^2 + 2|a_1 a_2| \sin\phi \tag{5.4}$$

$$|a_1 - ja_2|^2 = |a_1|^2 + |a_2|^2 - 2|a_1 a_2| \sin\phi \tag{5.5}$$

adding above two equations gives us the below equation:

$$|a_1 - ja_2|^2 - |a_1 + ja_2|^2 = 4|a_1 a_2| \cos\phi$$
$$\sin\phi = \frac{|a_1 - ja_2|^2 - |a_1 + ja_2|^2}{4|a_1 a_2|} \tag{5.6}$$

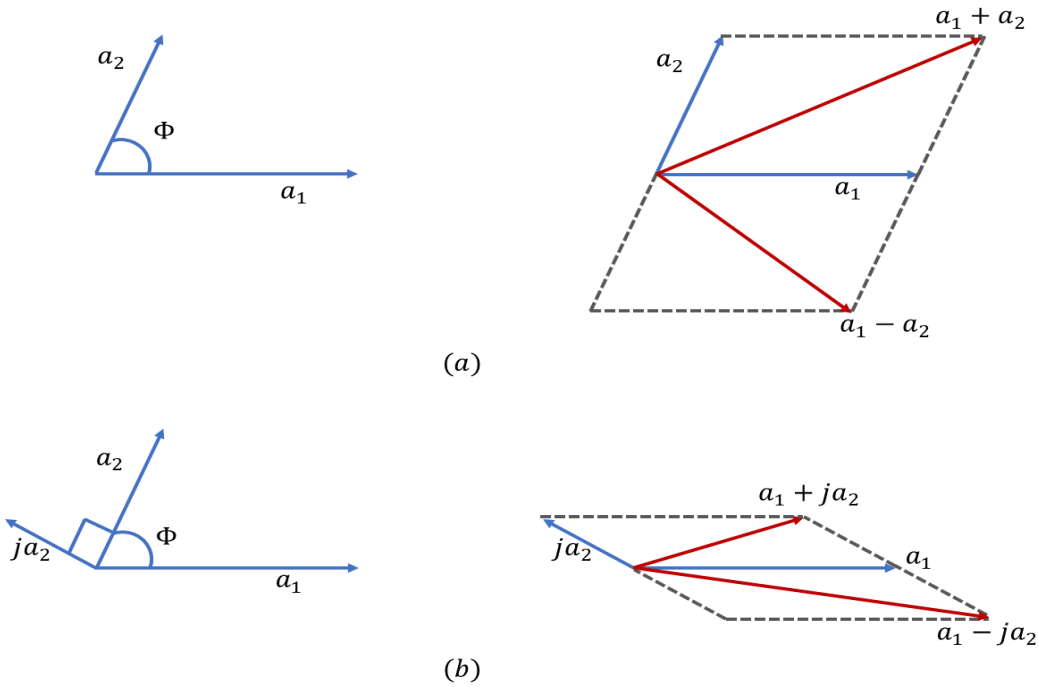

Figure 5.1 Basic idea behind six port reflectometer.

These required phase shift of $0°$, $90°$, $180°$ and $270°$ are achieved by utilising quadrature couplers, power dividers and there combination as described in the subsequent section.

5.2 Proposed Design and Methodology

The proposed IBNA overcomes the obstacles mentioned in the chapter 1 by utilising the concept of a Six-Port Reflectometer and an RF biosensor to detect various materials. While Fig. 1.3 depicts the basic architecture of the proposed IBNA, Fig. 5.2 provides a more detailed perspective to comprehend the

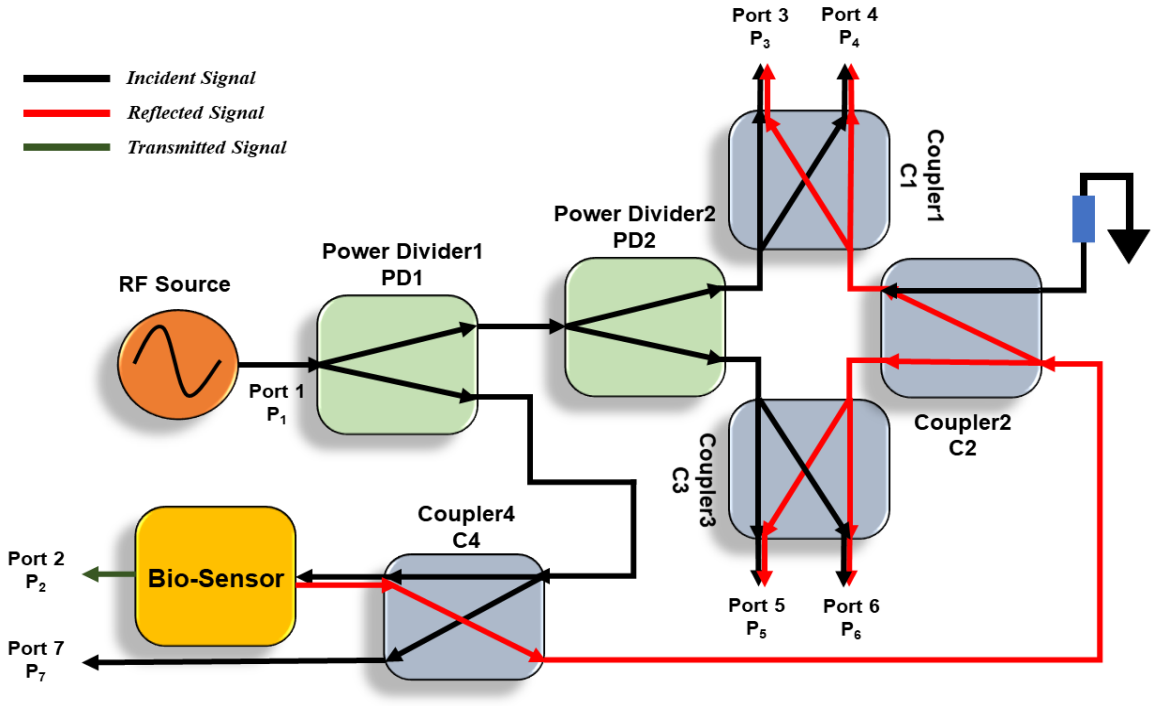

Figure 5.2 Detailed Block diagram of proposed dual-band integrated network.

IBNA's architecture. As previously stated, an IBNA combines a DBSPR and an RF biosensor. Hence, an IDC and CSRR based RF-bio liquid cavity has been designed and simulated as an RF biosensor to demonstrate the concept, whereas IDC has been fabricated for the purpose of experimentation.

The setup, as shown in Fig. 1.3, includes a frequency synthesiser that serves as an RF source and provides the system's input power, which is routed to the sensor. The sensor then reflects some of the input power back to the sensor, which then travels to the four ports (P_3 to P_6) via couplers and power dividers. The reflected power is detected by power detectors, and the data is then collected, processed, and displayed with MATLAB.
IBNA's design process is simplified, as illustrated in Fig. 5.3.

AD4351 has been used as an RF source in the proposed IBNA, operating in the frequency range of 35 MHz - 4500 MHz range. In addition, AD8318 power metres were used to measure the power received at ports $(P_3 - P_6)$. Since the RF source's operating range is limited, therefore the frequency of operation for IBNA must be set between 35 and 4500 MHz.

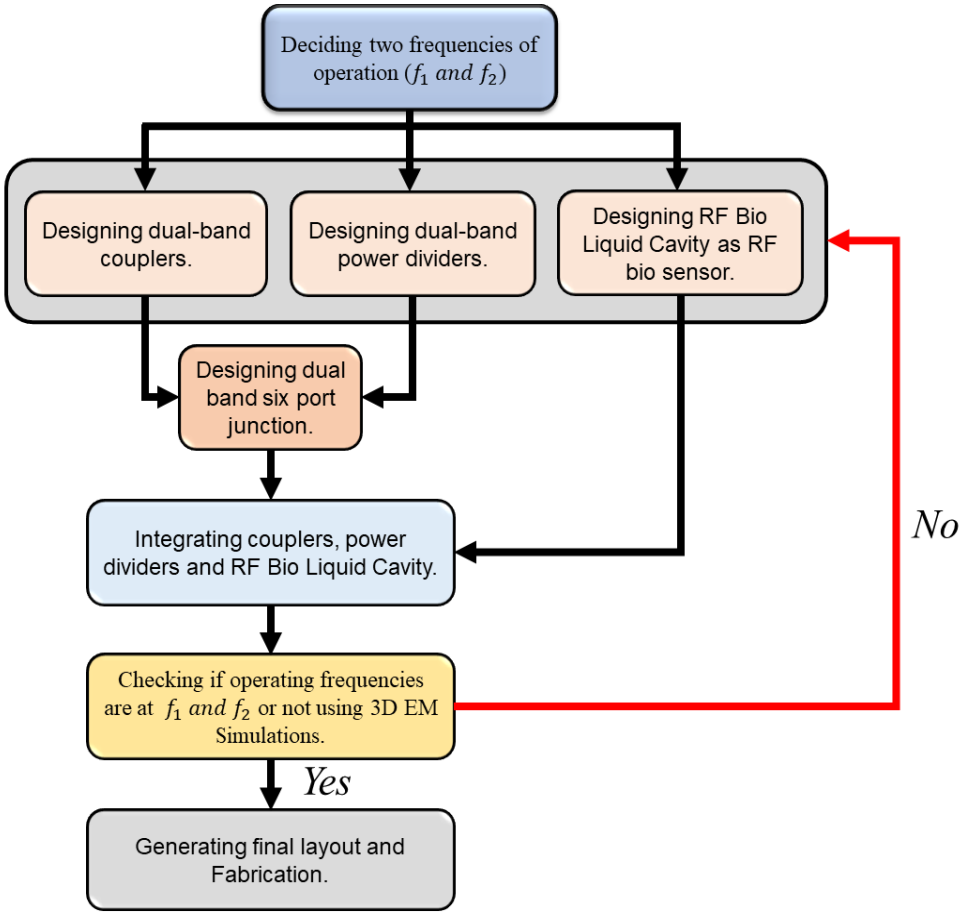

Figure 5.3 Block diagram of designing process for IBNA.

In this work, the operating frequencies of 1.1 GHz and 2.3 GHz are chosen for demonstration purposes. All components, such as power dividers and couplers, must operate within these two frequency bands. Furthermore, an IDC-based water-filled cavity operating at 2.2 GHz was designed. Water was used as a solvent in this case because it has a constant dielectric constant up to 10GHz [68]. A detailed description of each block's design procedure with simulation results is provided in the previous chapters.

5.2.1 Six Port Network

The Six-Port Network technique was first introduced by Engen and Hoer in the 1970s [23]. The Six port architecture is a passive structure with two input ports and four output ports, according to [69]. It is widely used as a communication receiver for microwave and millimetre wave frequencies, [70]. As previously stated, the six-port structure operates on the interferometric principle. As shown in Fig.

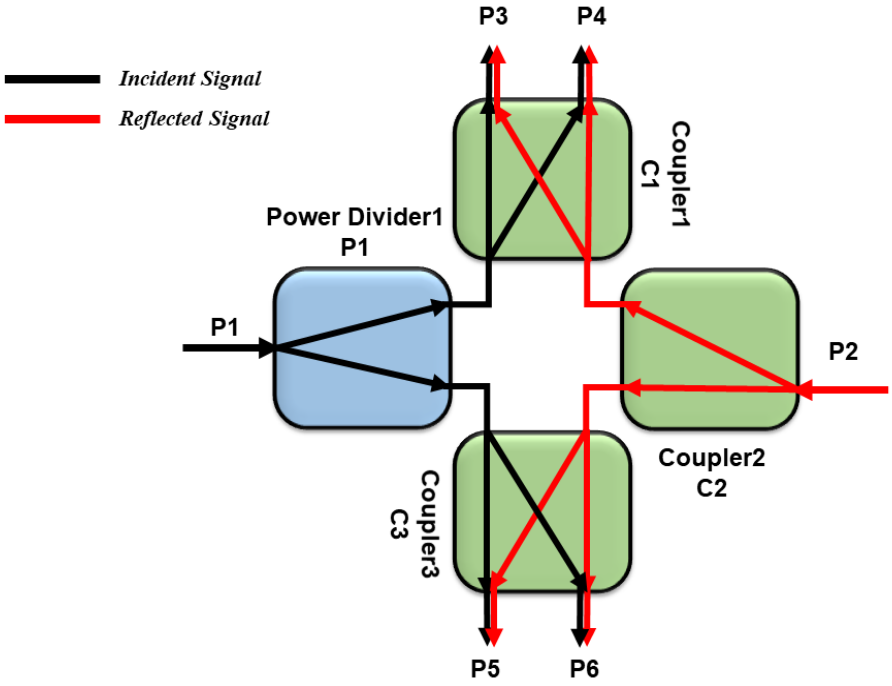

Figure 5.4 Block diagram of dual band six port junction.

5.4, the two input signals (P 1 and P 2) become superimposed, resulting in constructive and destructive interactions. The magnitude and phase of the two input signals will then determine the power received at the four output ports $(P3 - P4)$. The two input signals in a Six-Port Network are as follows:

$$P_1 = A_1.e^{j(2\pi ft+\phi_1)} \tag{5.7}$$

$$P_2 = A_2.e^{j(2\pi ft+\phi_2)} \tag{5.8}$$

Since the dual-band couplers introduce phase differences at the output ports [71], therefore the equations for the output ports can be written as follows:

$$P_3 = K.(P_1 - P_2) \tag{5.9}$$

$$P_4 = K.j(P_1 + P_2) \tag{5.10}$$

$$P_5 = K.(P_1 + jP_2) \tag{5.11}$$

$$P_6 = K.(jP_1 + P_2) \tag{5.12}$$

where, K is the constant due to division of power from couplers and power divider and, P_3, P_4, P_5 and P_6 are output signals received at four output ports respectively.

5.2.2 Simulation Results of Six Port Junction

Since Six Port Junction is at the core of the whole device as can be seen from Fig. 5.2. Therefore, the S-parameter of six port junction are important to observe before integrating the all the component together. Fig 5.5 shows s-parameters obtained by simulating the circuit as mention in the Fig. 5.4. Here, port 2 is one of the output ports.

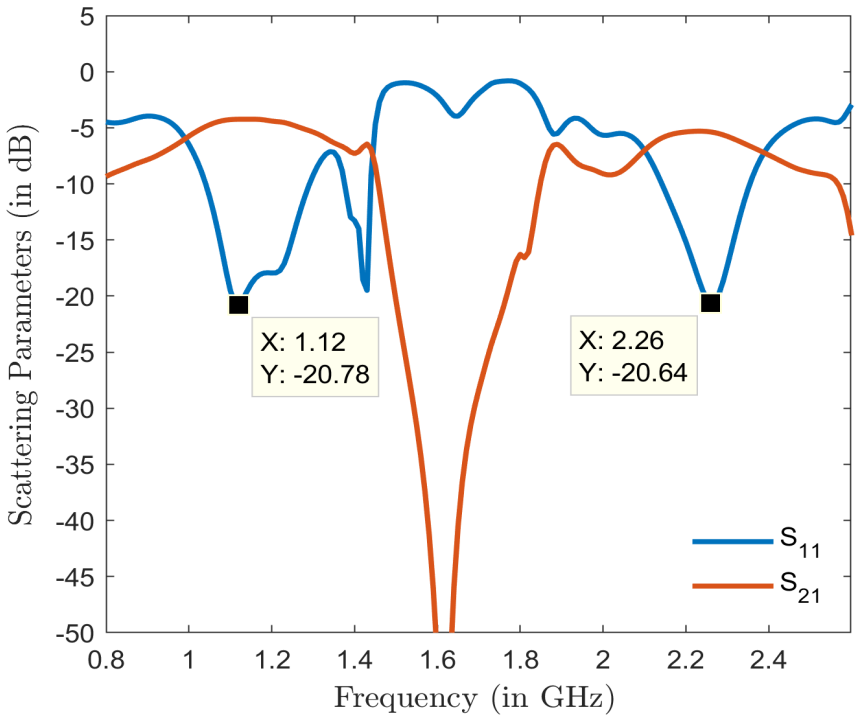

Figure 5.5 S-parameters for dual band Six Port Junction.

5.2.3 RF Bio sensing Liquid Cavity

For the purpose of testing of propsoed design, IBNA was designed and integrated with two different types of RF bio liquid cavities based on Inter Digitated Capacitance (IDC) and Complimentary Split

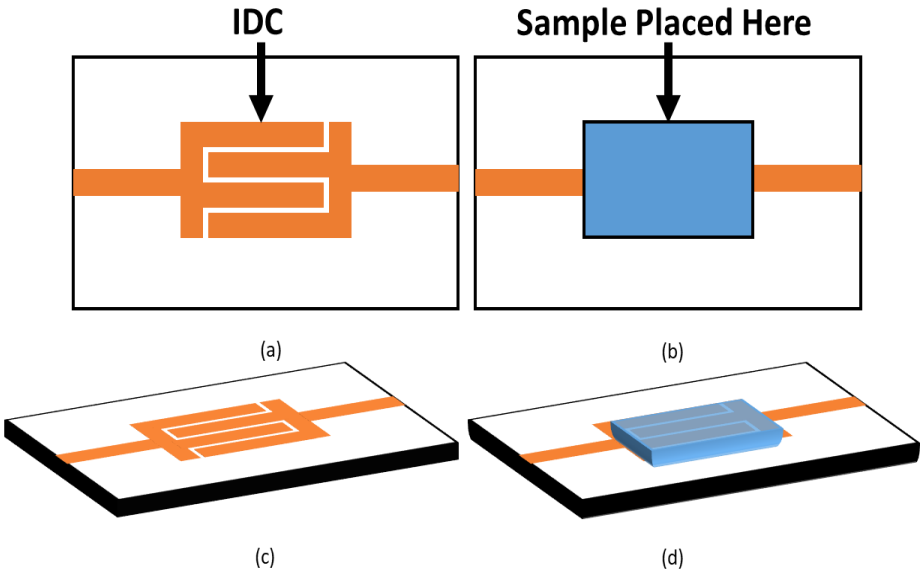

Figure 5.6 Inter-digitated Capacitance based RF bio Sensor: a) Top View, b) Top View with Sample, c) Bird Eye View, and d) Bird Eye view with Sample.

Ring Resonance (CSRR) for the measurement of shift in resonance frequency in transmission and reflection coefficients.
IDC and CSRR are one of the most common types of RF-based Sensors used in biochemical applications [72, 73], [19, 74–77]. A typical IDC-based sensor is made up of several fingers that are arranged in a regular pattern on top of a substrate. The number of fingers and the distance between them have a direct impact on the frequency response of the sensor. However, a CSRR-based sensor is made by ring made up of cavities on the metal surface with a feed line. A common ground is installed beneath the substrate, or co-planar ground lines are constructed on the substrate.

These sensors are quick, simple, and efficient, with low fabrication complexities and costs. They are distinguished by E-Field regions that are concentrated on the top of the fingers and in the gap between the fingers for IDC, similarly, in rings for CSRR. The presence of samples in these regions causes a change in the sensor's resonance characteristics. This shift can then be used to perform both qualitative and quantitative analysis on various materials under test. Some of the articles that discuss the design process of IDCs are [78–81].

The RF liquid Bio-Cavity has been designed and simulated for sensing purposes. The structure of the RF Bio Liquid-Cavity and the placement of the sample are depicted in Fig. 5.6, 5.7. Furthermore, Fig. 5.8 for IDC shows the reflection coefficient and resonant frequency shift when the sensor was loaded

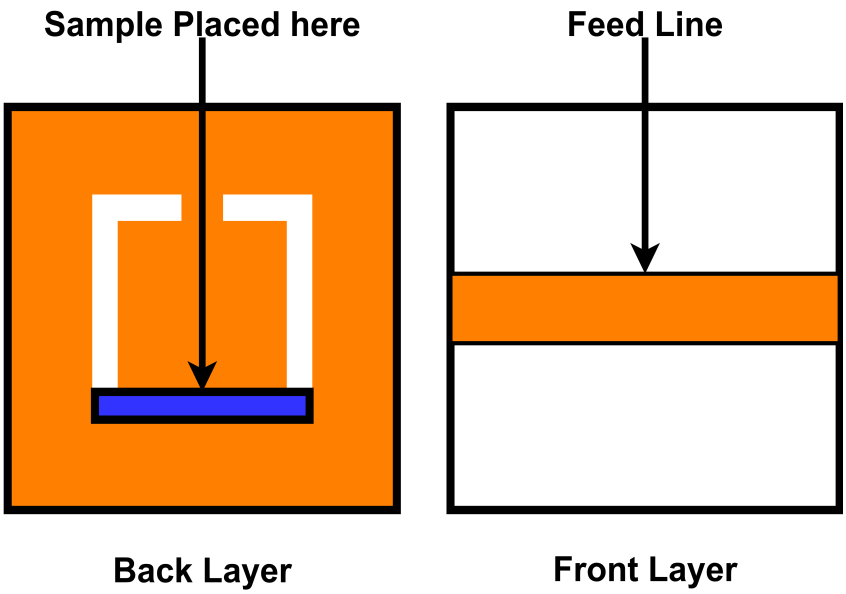

Figure 5.7 Complimentary Split Ring Resonator based RF bio Sensor: a) Top View, b) Top View with Sample.

with water, glucose, and sucrose. When the material was changed from water to Sucrose and Glucose, there was a 63 MHz and 93 MHz shift in resonant frequency, respectively. Similarly, Fig. 5.9 for CSRR.

As shown in Fig. 5.2, the devices mentioned in the previous chapters like couplers power dividers and RF bio-liquid cavity were integrated together and the input signal was generated by a frequency synthesizer module from Analog Device that consists of ADF4351. The coupler connected to the sensor helps pass the incident signal to the DUT and separates the reflected signal from the incident signal by transferring it to the six-port network's side. Furthermore, the six-port network's output ports (P_3 - P_6) are connected with Analog Devices power metre, i.e. AD8318, which measures the output power received. The power received is then processed using MATLAB to get the required plot. The magnitude of the reflection coefficient can then be calculated by using the following equation:

$$|s_{11}| = \frac{|(P_3 - P_4) + j(P_5 - P_6)|}{|P_7|} \tag{5.13}$$

where, P_3 - P_7 are the power at their respective ports. It should be noted that although the above equation can be utilised to measure phase as well, the focus of this paper will only be on magnitude.

Similarly, the transmission coefficient can also be measured by using the below equation:

$$|s_{21}| = |\frac{P_8}{P_7}| \tag{5.14}$$

5.3 Experimental Setup, Simulation and Measurement Results

This section consists all the simulation results and experimental results performed with IBNA. It is important to note here that the experiments were performed with IDC based RF bio liquid cavity.

5.3.1 Simulation Results for IBNA

The simulation mimicked the practical method of changing materials with different permittivity over the designed RF-Bio liquid cavity. As, stated earlier, the simulations were performed by integrating IBNA with two different types of RF Bi-liquid cavities out of which one is based on CSRR and another one is based on IDC. Fig. 5.12 and 5.14 shows the above setup with Layouts in CSRR and IDC respectively. Fig. 5.10 and Fig. 5.11 presents simulation results for IDC and CSRR integrated with IBNA. It can be observed that using IBNA with both the RF cavities whenever the material was changed the resonant frequency shifted from its initial frequency.

5.3.2 Experimental Setup and Measurement Results

The experimental setup for IBNA is depicted in Fig. 5.15. As shown in the figure an RF source i.e Frequency synthesiser (ADF4351) was used, which generates frequencies ranging from 30 MHz to 4500 MHz [82]. In addition, AD8318 [83] was used as a power detector to measure power received at their respective ports. Furthermore, the data of power measured from the four ports was transferred to MATLAB, and final plots were generated. It should be noted that the volume of the samples and temperature of the room was kept constant at 400 μl and 25°C respectively while performing these experiments.

For performing the experiment the following materials with different permittivity were chosen:

1. Distilled Water (ϵ_w= 79).
2. Sucrose (ϵ_s =74).
3. Glucose (ϵ_g = 72).

The permittivity of each material is represented by ϵ_w, ϵ_s and ϵ_g. For testing, 1 M solutions of glucose and sucrose in water were employed, with 400 μl of the liquids being gently dropped over the IDC's sensitive area. When the RF-Bio liquid cavity was loaded with water, a resonant frequency of 2483 MHz was reached, as shown in Fig. 5.16. However, a shift of 15 MHz and 20 MHz was detected when the substance was changed from water to sucrose and glucose, respectively.

In Table. 5.1, the suggested IBNA has been compared to other published solutions to show its benefits. It is demonstrated that IBNA has the simplest design. It also has the distinct feature of having built-in sensing and measurement systems, which no other design possess.

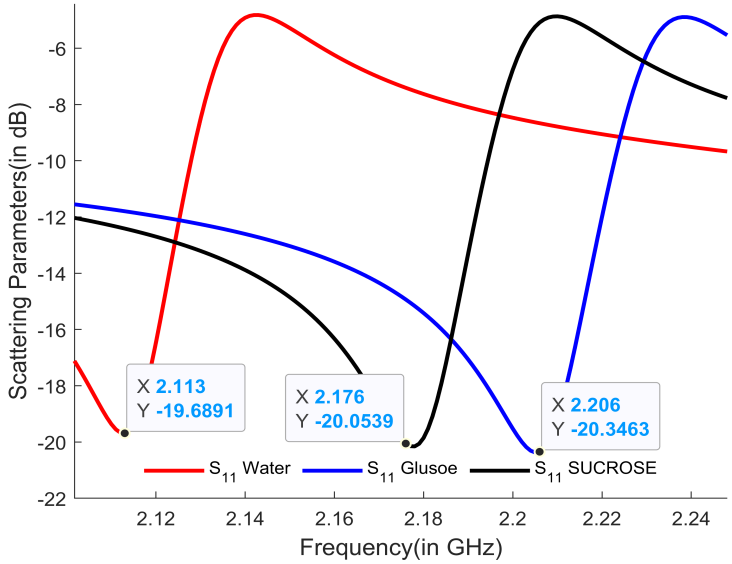

Figure 5.8 S-parameter for IDC based RF bio liquid cavity.

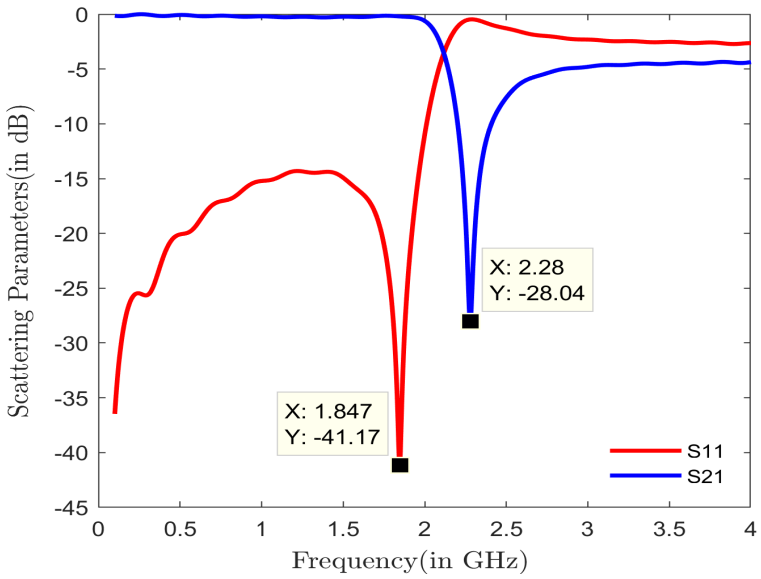

Figure 5.9 S-parameter for CSRR based RF bio liquid cavity.

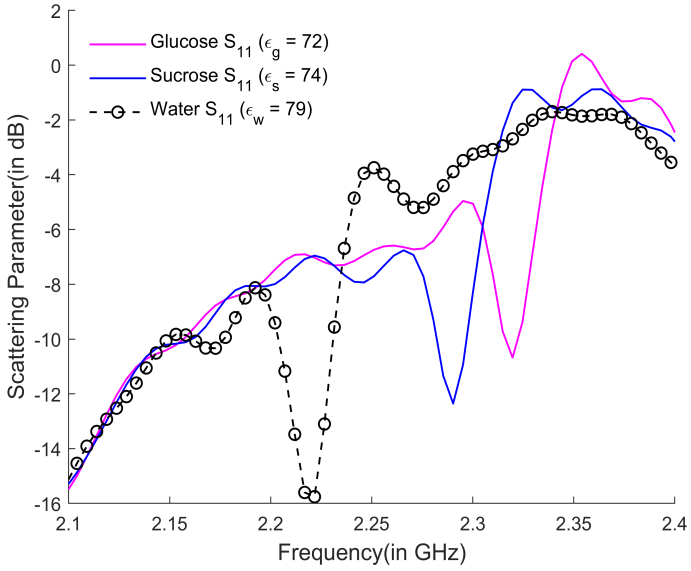

Figure 5.10 Scattering parameter achieved using simulation for IBNA integrated with IDC for different MUTs (with different permittivity) having 1 Molar concentration.

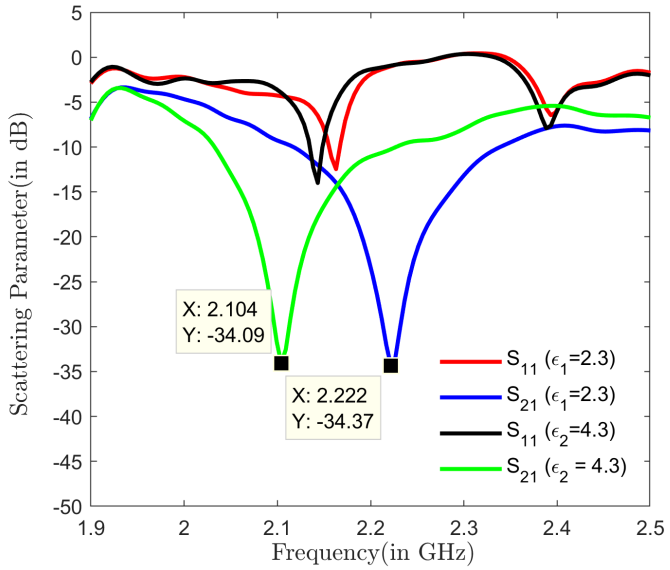

Figure 5.11 Scattering parameter achieved using simulation for IBNA integrated with CSRR for different MUTs (with different permittivity).

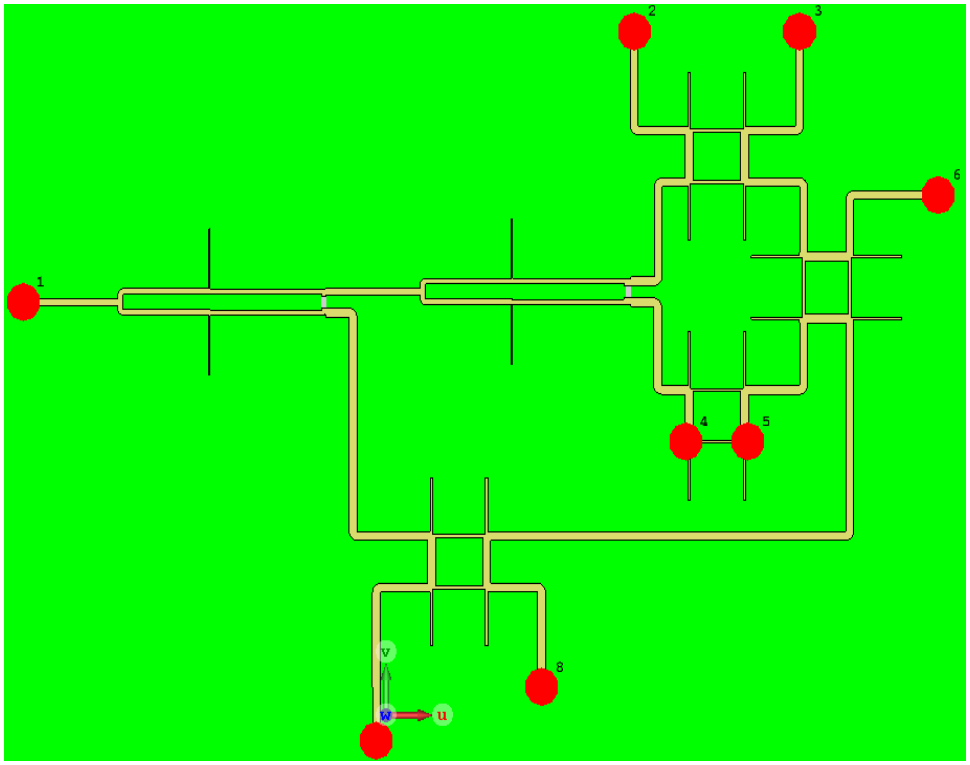

Figure 5.12 Layout of IBNA with CSRR based RF cavity.

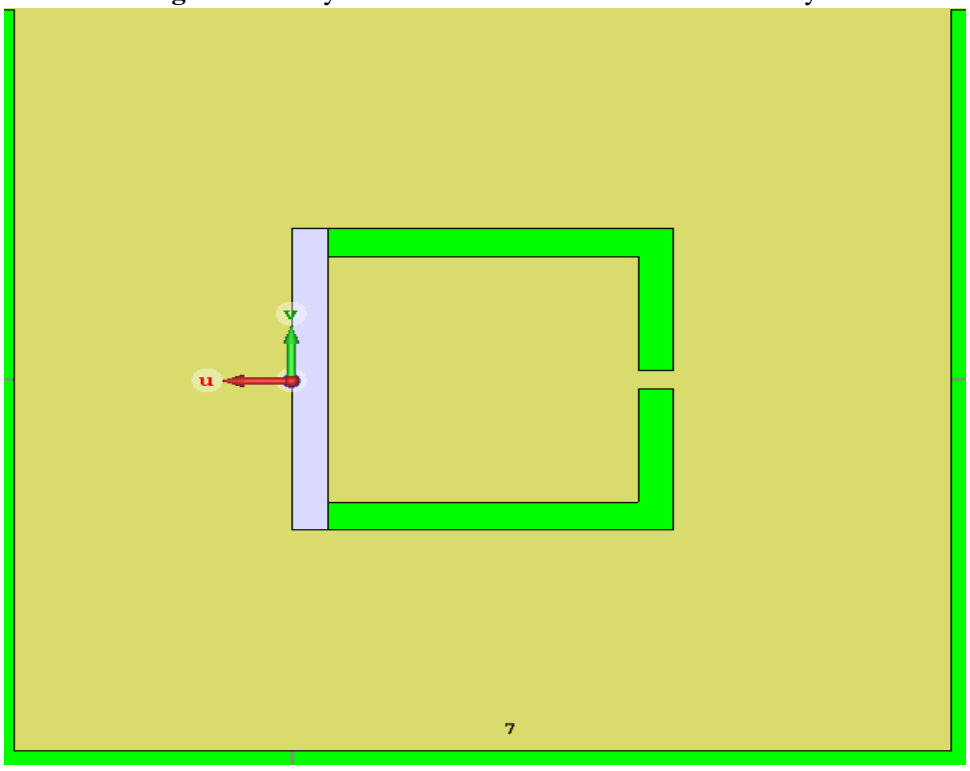

Figure 5.13 CSRR based RF cavity attached with IBNA in in CST 3D EM simulator.

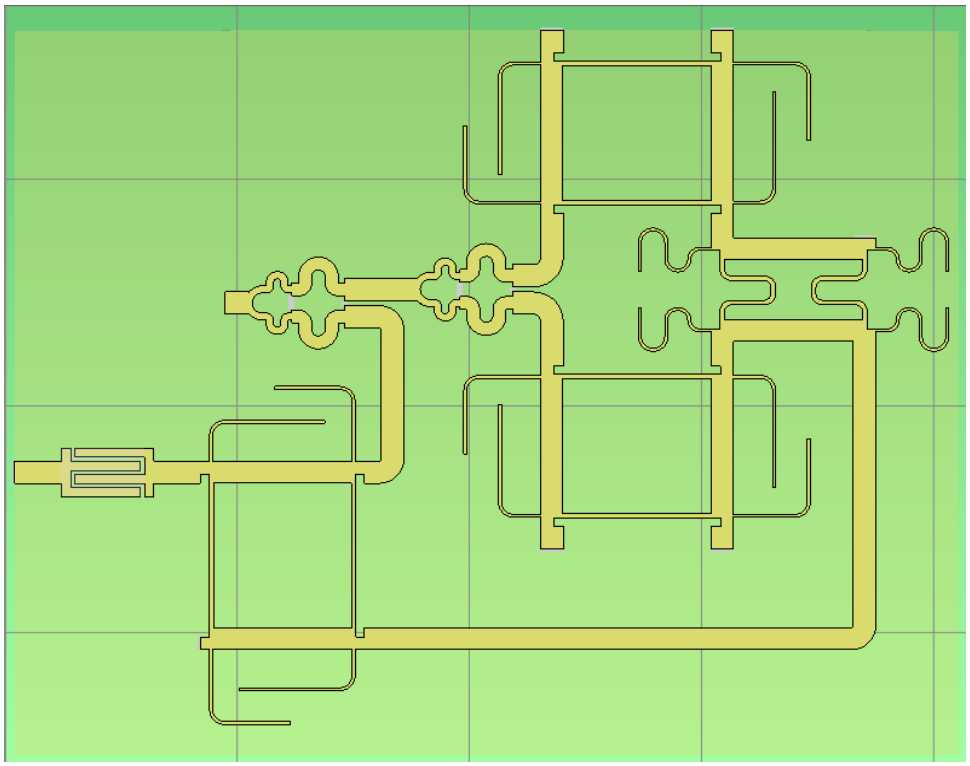

Figure 5.14 Layout of IBNA with IDC based RF cavity in CST 3D EM simulator.

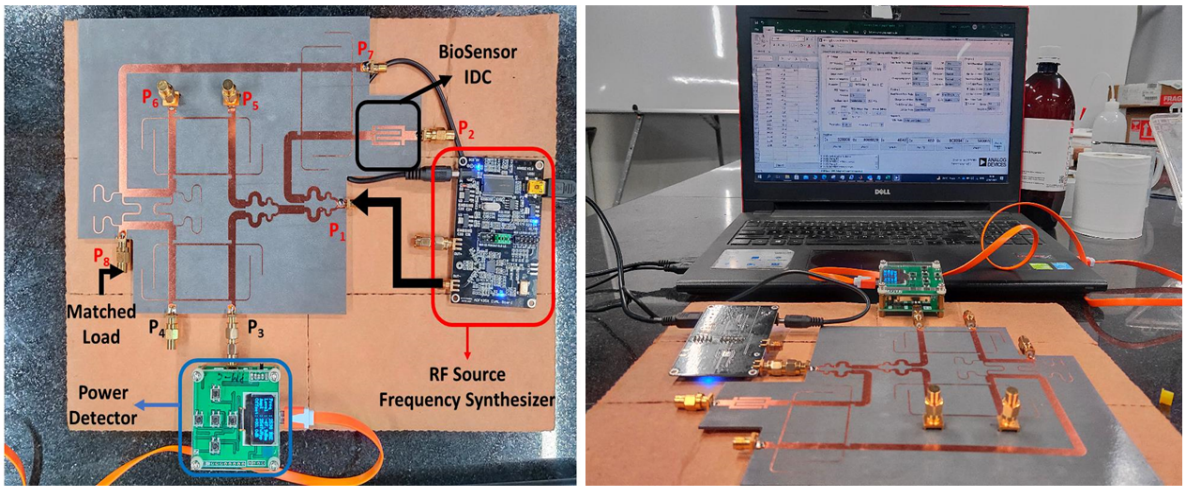

Figure 5.15 Experimental setup of fabricated IBNA with power detectors and frequency synthesizers.

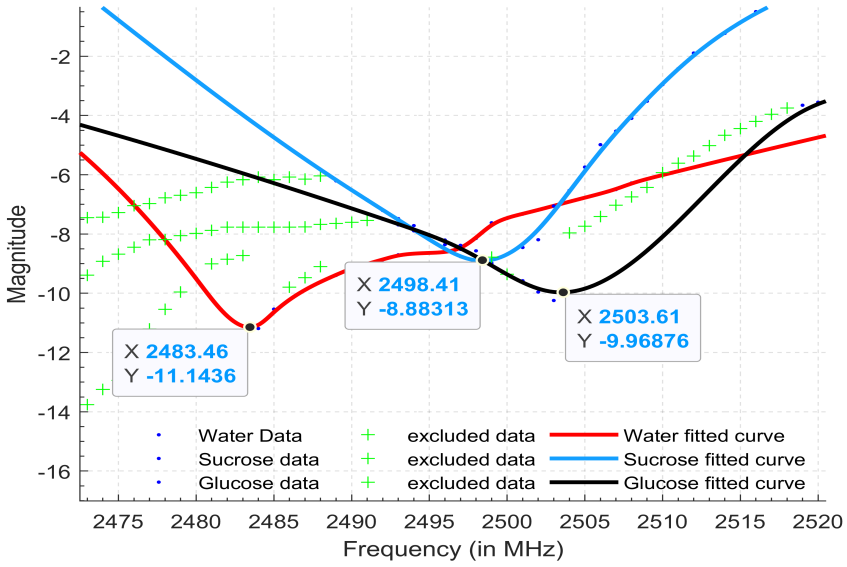

Figure 5.16 Experimental results using glucose, sucrose and water.

Parameters	[84]	[85]	[86]	[87]	[88]	[70]	[89]	This Work
Application	general purpose	general purpose	permittivity sensor	CW Radar	communi-cation receiver	CW Radar	general purpose	permittivity sensor
Frequency range (GHz)	2.5-3.5	55-65	1.9-2.058, 15.2-16.6	24	2.45	75-84	1-10	1.05-1.3, 2.14 - 2.35
Bandwidth ratio (f_1/f_2)	1.4	1.18	1.09	1	1	1.12	10	1.23, 1.19
Technology	PCB Stripline	MHMIC	MEMS	PCB Microstrip line	PCB Microstrip line	SiGe MMIC	PCB Microstrip line	PCB Microstrip line
Size (mm× mm)	56× 49	15×15	6.8×50 with VCO, Power Detector, Sensor	-	-	1.03×1.13 with Power Detector, LNA	-	150×130
Topology	multi detector	multi detector	multi-state reflec-tometer	multi detector	multi detector	multi detector	multi detector	multi detector
No. of Power Detector	4	4	1	4	2	4	2	4
Design complex-ity	medium	medium	high	medium	medium	high	medium	low

Table 5.1 Comparison table of multiport reflectometers performance.

Chapter 6

Conclusions

The capacity of a Dual-Band SPR to quantify the magnitude of the reflected and transmitted signal, and shift in resonant frequency was investigated. Furthermore, by combining power dividers, couplers, and an RF bio liquid cavity with DBSPR, a generalised strategy for the construction of an Integrated Bio-Sensing Network Analyser was established. When different permittivity materials were used as the Material Under Test, the proposed device detected and measured the shift in resonance frequencies (MUT). The findings were encouraging, indicating that this method could be a viable and cost-effective alternative for biochemical applications. However, several issues remain, such as a large form factor at low frequencies and a wider bandwidth. Moreover, the precision of the proposed device is also dependent on the RF source's quality and the noise figure in the power detectors.

Future work includes dealing with the above challenges and exploring the effects of volume and concentration of the material under test on the response of the designed system.

Related Publications

Conference:

1. M. Awasthi, K. Wadhwani, A. Syed and M. Hashmi, " Dual-Band Integrated Network Analyzer For RF Bio Sensing Application," 2020 IEEE Asia-Pacific Microwave Conference (APMC), 2020, pp. 196-198, doi: 10.1109/APMC47863.2020.9331610.

Journal:

1. Mayank Awasthi, Annesha Mazumder, Azeemuddin Syed, Mohammad Hashmi. **A Dual-Band Integrated Network Analyzer For Water Solvent specific RF Bio Sensors** in *"IEEE Sensors Journal", 2022. [To be submitted]*

Bibliography

[1] N.D. Booth, J.C. ad Orloff, J. Mateu, M. Janezic, M. Rinehart, and J.A. Beall. Quantitative permittivity measurements of nanoliter liquid volumes in microfluidic channels to 40 ghz. *IEEE Transactions on Instrumentation and Measurement*, 59(12):3279–3288, 2010.

[2] J. Mateu, N. Orloff, M. Rinehart, and J.C. Booth. Broadband permittivity of liquids extracted from transmission line measurements of microfluidic channels. In *2007 IEEE/MTT-S International Microwave Symposium*, pages 523–526. IEEE, 2007.

[3] I. Ocket, L. Song, D. Grillet, B. Embrechts, D. Schreurs, W. De Raedt, and B. Nauwelaers. Dielectric characterization of biological liquids and tissues up to 110 ghz using an ltcc cpw sensor. In *2013 IEEE Topical Conference on Biomedical Wireless Technologies, Networks, and Sensing Systems*, pages 43–45. IEEE, 2013.

[4] D. Elsheakh, H. Elsadek, E. Abdullah, S. Atteya, and W.N. ELmazny. Novel rapid detection of different viruses in blood using microimmuno-sensor. In *2013 7th European Conference on Antennas and Propagation (EuCAP)*, pages 1128–1131. IEEE, 2013.

[5] R. Narang, S. Mohammadi, M.M. Ashani, H. Sadabadi, H. Hejazi, M.H. Zarifi, and A. Sanati-Nezhad. Sensitive, real-time and non-intrusive detection of concentration and growth of pathogenic bacteria using microfluidic-microwave ring resonator biosensor. *Scientific reports*, 8(1):1–10, 2018.

[6] H.J. Lee, J.H. Lee, H.S. Moon, I.S. Jang, J.S. Choi, J.G. Yook, and H.I. Jung. A planar split-ring resonator-based microwave biosensor for label-free detection of biomolecules. *Sensors and Actuators B: Chemical*, 169:26–31, 2012.

[7] M. Nikolic-Jaric, S.F. Romanuik, G.A. Ferrier, G.E. Bridges, M. Butler, K. Sunley, D.J. Thomson, and M.R. Freeman. Microwave frequency sensor for detection of biological cells in microfluidic channels. *Biomicrofluidics*, 3(3):034103, 2009.

[8] K. Grenier, D. Dubuc, P.E. Poleni, M. Kumemura, H. Toshiyoshi, T. Fujii, and H. Fujita. Resonant based microwave biosensor for biological cells discrimination. In *2010 IEEE Radio and Wireless Symposium (RWS)*, pages 523–526. IEEE, 2010.

[9] L.Y. Zhang, C.B.M. Du Puch, A. Lacroix, C. Dalmay, A. Pothier, C. Lautrette, S. Battu, F. Lalloué, M.O. Jauberteau, and P. Blondy. Microwave biosensors for identifying cancer cell aggressiveness grade. In *2012 IEEE/MTT-S International Microwave Symposium Digest*, pages 1–3. IEEE, 2012.

[10] Azadeh Peyman, Bor Kos, Mihajlo Djokić, Blaž Trotovšek, Clara Limbaeck-Stokin, Gregor Serša, and Damijan Miklavčič. Variation in dielectric properties due to pathological changes in human liver. *Bioelectromagnetics*, 36(8):603–612, 2015.

[11] H.W. Wu. Label-free and antibody-free wideband microwave biosensor for identifying the cancer cells. *IEEE Transactions On Microwave Theory And Techniques*, 64(3):982–990, 2016.

[12] C. Dalmay, J. Leroy, A. Pothier, and P. Blondy. Development of high frequency microfluidic biosensors for intracellular analysis. *Procedia Engineering*, 87:54–57, 2014.

[13] N.M. née Haase, Trieu Fuge, G., A.P. H.K., Zeng, and A.F. Jacob. Miniaturized transmission-line sensor for broadband dielectric characterization of biological liquids and cell suspensions. *IEEE Transactions on Microwave Theory and Techniques*, 63(10):3026–3033, 2015.

[14] Annesha Mazumder, Syed Azeemuddin, Tapan K Sau, and Prabhakar Bhimalapuram. Study of gold particles in hfss with varying physical parameters and arrangements. In *2020 IEEE 15th International Conference on Nano/Micro Engineered and Molecular System (NEMS)*, pages 529–532. IEEE, 2020.

[15] Annesha Mazumder, Syed Azeemuddin, Tapan K Sau, and Prabhakar Bhimalapuram. Role of shape of gold nanoparticles in sensing biomolecules using radio-frequency based sensors. In *2020 IEEE Sensors*, pages 1–4. IEEE, 2020.

[16] Rowan Gilmore and Les Besser. *Practical RF Circuit Design for Modern Wireless Systems: Active Circuits and Systems, Volume 2*, volume 1. Artech House, 2003.

[17] Junho Yeo and Jong-Ig Lee. High-sensitivity microwave sensor based on an interdigital-capacitor-shaped defected ground structure for permittivity characterization. *Sensors*, 19(3):498, 2019.

[18] Amyrul Azuan Mohd Bahar, Z Zakaria, MK Md Arshad, AAM Isa, Y Dasril, and Rammah A Alahnomi. Real time microwave biochemical sensor based on circular siw approach for aqueous dielectric detection. *Scientific reports*, 9(1):1–12, 2019.

[19] Mohammad Arif Hussain Ansari, Abhishek Kumar Jha, and Mohammad Jaleel Akhtar. Design and application of the csrr-based planar sensor for noninvasive measurement of complex permittivity. *IEEE Sensors Journal*, 15(12):7181–7189, 2015.

[20] Dang Khoa Huynh and Gernot Zimmer. Reflectometer with complete error correction. In *2018 International Conference on Advanced Technologies for Communications (ATC)*, pages 133–141. IEEE, 2018.

[21] Johannes Nehring, Martin Schütz, Marco Dietz, Ismail Nasr, Klaus Aufinger, Robert Weigel, and Dietmar Kissinger. Highly integrated 4–32-ghz two-port vector network analyzers for instrumentation and biomedical applications. *IEEE Transactions on Microwave Theory and Techniques*, 65(1):229–244, 2016.

[22] Ismail Nasr, Johannes Nehring, Klaus Aufinger, Georg Fischer, Robert Weigel, and Dietmar Kissinger. Single-and dual-port 50-100-ghz integrated vector network analyzers with on-chip dielectric sensors. *IEEE Transactions on Microwave Theory and Techniques*, 62(9):2168–2179, 2014.

[23] Glenn F Engen and Cletus A Hoer. Application of an arbitrary 6-port junction to power-measurement problems. *IEEE transactions on Instrumentation and Measurement*, 21(4):470–474, 1972.

[24] Cletus A Hoer. The six-port coupler: A new approach to measuring voltage, current, power, impedance, and phase. *IEEE Transactions on Instrumentation and Measurement*, 21(4):466–470, 1972.

[25] Glenn F Engen. The six-port reflectometer: An alternative network analyzer. *IEEE Transactions on microwave theory and techniques*, 25(12):1075–1080, 1977.

[26] Glenn F Engen. *Microwave circuit theory and foundations of microwave metrology*. Number 9. IET, 1992.

[27] FM Ghannouchi, Y Xu, and RG Bosisio. One-step connection method for the measurement of n-port microwave networks using six-port techniques. *IEE Proceedings-Microwaves, Antennas and Propagation*, 141(4):285–289, 1994.

[28] S Linz, M Hofmann, G Fischer, R Weigel, and D Kissinger. A multiband 2-port vector network analyzer based on six-port junctions for biomedical measurement applications between 6 ghz and 33 ghz. In *2013 IEEE-APS Topical Conference on Antennas and Propagation in Wireless Communications (APWC)*, pages 532–535. IEEE, 2013.

[29] David M Pozar. *Microwave engineering*. John wiley & sons, 2011.

[30] George D Vendelin, Anthony M Pavio, Ulrich L Rohde, and Matthias Rudolph. *Microwave circuit design using linear and nonlinear techniques*. John Wiley & Sons, 2021.

[31] Matthew NO Sadiku et al. *Elements of electromagnetics*, volume 428. Oxford university press New York, 2001.

[32] Leo Maloratsky. *Passive RF and microwave integrated circuits*. Elsevier, 2003.

[33] Mi Zhou, Jin Shao, Bayaner Arigong, Han Ren, Rongguo Zhou, and Hualiang Zhang. A varactor based 90° directional coupler with tunable coupling ratios and reconfigurable responses. *IEEE transactions on microwave theory and techniques*, 62(3):416–421, 2014.

[34] Jia-Lin Li and Bing-Zhong Wang. Novel design of wilkinson power dividers with arbitrary power division ratios. *IEEE Transactions on Industrial Electronics*, 58(6):2541–2546, 2010.

[35] I-Hsiang Lin, Marc DeVincentis, Christophe Caloz, and Tatsuo Itoh. Arbitrary dual-band components using composite right/left-handed transmission lines. *IEEE Transactions on Microwave Theory and Techniques*, 52(4):1142–1149, 2004.

[36] K-KM Cheng and Fai-Leung Wong. A novel approach to the design and implementation of dual-band compact planar 90/spl deg/branch-line coupler. *IEEE Transactions on Microwave Theory and Techniques*, 52(11):2458–2463, 2004.

[37] Kwok-Keung M Cheng and Sung Yeung. A novel dual-band 3-db branch-line coupler design with controllable bandwidths. *IEEE transactions on microwave theory and techniques*, 60(10):3055–3061, 2012.

[38] Hualiang Zhang and Kevin J Chen. A stub tapped branch-line coupler for dual-band operations. *IEEE Microwave and wireless components letters*, 17(2):106–108, 2007.

[39] Han Ren, Jin Shao, Mi Zhou, Bayaner Arigong, Jun Ding, and Hualiang Zhang. Design of dual-band transmission line with flexible phase shifts and its applications. *Electronics Letters*, 51(3):261–262, 2015.

[40] Kuo-Sheng Chin, Ken-Min Lin, Yen-Hsiu Wei, Tzu-Hao Tseng, and Yu-Jie Yang. Compact dual-band branch-line and rat-race couplers with stepped-impedance-stub lines. *IEEE Transactions on Microwave Theory and Techniques*, 58(5):1213–1221, 2010.

[41] Ching-Luh Hsu, Jen-Tsai Kuo, and Chin-Wei Chang. Miniaturized dual-band hybrid couplers with arbitrary power division ratios. *IEEE transactions on microwave theory and techniques*, 57(1):149–156, 2008.

[42] Erick Emmanuel Djoumessi, Eric Marsan, Christophe Caloz, Mohamed Chaker, and KE Wu. Varactor-tuned dual-band quadrature hybrid coupler. *IEEE Microwave and Wireless Components Letters*, 16(11):603–605, 2006.

[43] Qiang Liu, Yuan'an Liu, Yongle Wu, Jun-Yu Shen, Shulan Li, Cuiping Yu, and Ming Su. Generalized impedance-transforming dual-band branch-line couplers for arbitrary coupling levels. *Progress In Electromagnetics Research B*, 53:399–415, 2013.

[44] Pei-Ling Chi and Kuan-Lin Ho. Design of dual-band coupler with arbitrary power division ratios and phase differences. *IEEE Transactions on Microwave Theory and Techniques*, 62(12):2965–2974, 2014.

[45] Lap K Yeung. A compact dual-band 90° coupler with coupled-line sections. *IEEE transactions on microwave theory and techniques*, 59(9):2227–2232, 2011.

[46] Chun-Han Yu and Yi-Hsin Pang. Dual-band unequal-power quadrature branch-line coupler with coupled lines. *IEEE Microwave and Wireless Components Letters*, 23(1):10–12, 2012.

[47] Xi Wang, Wen-Yan Yin, and Ke-Li Wu. A dual-band coupled-line coupler with an arbitrary coupling coefficient. *IEEE transactions on microwave theory and techniques*, 60(4):945–951, 2012.

[48] Yongle Wu, Shao Yong Zheng, Sai-Wing Leung, Yuanan Liu, and Quan Xue. An analytical design method for a novel dual-band unequal coupler with four arbitrary terminated resistances. *IEEE Transactions on Industrial Electronics*, 61(10):5509–5516, 2014.

[49] Hyunchul Kim, Byungje Lee, and Myun-Joo Park. Dual-band branch-line coupler with port extensions. *IEEE transactions on microwave theory and techniques*, 58(3):651–655, 2010.

[50] Yuk Shing Wong, Shao Yong Zheng, and Wing Shing Chan. Multifolded bandwidth branch line coupler with filtering characteristic using coupled port feeding. *Progress In Electromagnetics Research*, 118:17–35, 2011.

[51] Gordon P Riblet. A directional coupler with very flat coupling. *IEEE transactions on Microwave Theory and Techniques*, 26(2):70–74, 1978.

[52] Karun Rawat, Mohammed S Hashmi, and Fadhel M Ghannouchi. Dual-band rf circuits and components for multi-standard software defined radios. *IEEE Circuits and Systems Magazine*, 12(1):12–32, 2012.

[53] Canan Toker, Mustafa Saglam, Mustafa Ozme, and Nilgun Gunalp. Branch-line couplers using unequal line lengths. *IEEE Transactions on Microwave Theory and Techniques*, 49(4):718–721, 2001.

[54] Mohammad A Maktoomi, Mohammad S Hashmi, and Fadhel M Ghannouchi. Systematic design technique for dual-band branch-line coupler using t-and pi-networks and their application in novel wideband-ratio crossover. *IEEE Transactions on Components, Packaging and Manufacturing Technology*, 6(5):784–795, 2016.

[55] Tian Qiang, Cong Wang, and Nam-Young Kim. A compact high-reliability high-performance 900-mhz wpd using gaas-ipd technology. *IEEE Microwave and Wireless Components Letters*, 26(7):498–500, 2016.

[56] Yongle Wu, Zheng Zhuang, Yuanan Liu, Li Deng, and Zabih Ghassemlooy. Wideband filtering power divider with ultra-wideband harmonic suppression and isolation. *IEEE Access*, 4:6876–6882, 2016.

[57] Yu-Ann Lai, Chi-Ming Lin, Jui-Chieh Chiu, Che-Hung Lin, and Yeong-Her Wang. A compact ka-band planar three-way power divider. *IEEE microwave and wireless components letters*, 17(12):840–842, 2007.

[58] Yongle Wu, Yuanan Liu, Yaxing Zhang, Jinchun Gao, and Hui Zhou. A dual band unequal wilkinson power divider without reactive components. *IEEE Transactions on Microwave Theory and Techniques*, 57(1):216–222, 2008.

[59] Myun-Joo Park and Byungje Lee. A dual-band wilkinson power divider. *IEEE Microwave and Wireless Components Letters*, 18(2):85–87, 2008.

[60] Fu-Xing Liu, Yang Wang, Xiao-Yu Zhang, Chun-He Quan, and Jong-Chul Lee. A size-reduced triband gysel power divider with ultra-wideband harmonics suppression performance. *IEEE Access*, 6:34198–34205, 2018.

[61] Kwok-Keung M Cheng and Fai-Leung Wong. A new wilkinson power divider design for dual band application. *IEEE microwave and wireless components letters*, 17(9):664–666, 2007.

[62] Mohsen Hayati, Seyed-Ali Malakooti, and Ashkan Abdipour. A novel design of triple-band gysel power divider. *IEEE transactions on microwave theory and techniques*, 61(10):3558–3567, 2013.

[63] Myun-Joo Park. Dual-band wilkinson divider with coupled output port extensions. *IEEE transactions on microwave theory and techniques*, 57(9):2232–2237, 2009.

[64] Yongle Wu, Yuanan Liu, and Quan Xue. An analytical approach for a novel coupled-line dual-band wilkinson power divider. *IEEE Transactions on Microwave Theory and Techniques*, 59(2):286–294, 2010.

[65] Xiaolong Wang, Zhewang Ma, and Masataka Ohira. Theory and experiment of two-section two-resistor wilkinson power divider with two arbitrary frequency bands. *IEEE Transactions on Microwave Theory and Techniques*, 66(3):1291–1300, 2017.

[66] Mitchai Chongcheawchamnan, Sumongkol Patisang, Monai Krairiksh, and Ian D Robertson. Triband wilkinson power divider using a three-section transmission-line transformer. *IEEE Microwave and Wireless Components Letters*, 16(8):452–454, 2006.

[67] Fu-Xing Liu and Jong-Chul Lee. Design of new dual-band wilkinson power dividers with simple structure and wide isolation. *IEEE Transactions on Microwave Theory and Techniques*, 67(9):3628–3635, 2019.

[68] Andrei Andryieuski, Svetlana M Kuznetsova, Sergei V Zhukovsky, Yuri S Kivshar, and Andrei V Lavrinenko. Water: Promising opportunities for tunable all-dielectric electromagnetic metamaterials. *Scientific reports*, 5(1):1–9, 2015.

[69] Fadhel M Ghannouchi and Abbas Mohammadi. *The six-port technique with microwave and wireless applications*. Artech House, 2009.

[70] Benjamin Laemmle, Gabor Vinci, Linus Maurer, Robert Weigel, and Alexander Koelpin. A 77-ghz sige integrated six-port receiver front-end for angle-of-arrival detection. *IEEE Journal of Solid-State Circuits*, 47(9):1966–1973, 2012.

[71] Alexander Koelpin, Gabor Vinci, Benjamin Laemmle, Dietmar Kissinger, and Robert Weigel. The six-port in modern society. *IEEE Microwave Magazine*, 11(7):35–43, 2010.

[72] Jun Wan Kim. *Development of interdigitated capacitor sensors for direct and wireless measurements of the dielectric properties of liquids*. The University of Texas at Austin, 2008.

[73] E Hammerstad and O Jensen. Accurate models for microstrip computer-aided design. In *1980 IEEE MTT-S International Microwave Symposium Digest*, pages 407–409. IEEE, 1980.

[74] Chieh-Sen Lee and Chin-Lung Yang. Single-compound complementary split-ring resonator for simultaneously measuring the permittivity and thickness of dual-layer dielectric materials. *IEEE Transactions on Microwave Theory and Techniques*, 63(6):2010–2023, 2015.

[75] Manisha Shete, Makkattary Shaji, and Mohammad Jaleel Akhtar. Design of a coplanar sensor for rf characterization of thin dielectric samples. *IEEE Sensors Journal*, 13(12):4706–4715, 2013.

[76] Chieh-Sen Lee and Chin-Lung Yang. Thickness and permittivity measurement in multi-layered dielectric structures using complementary split-ring resonators. *IEEE Sensors Journal*, 14(3):695–700, 2013.

[77] Euclides Lourenço Chuma, Yuzo Iano, Glauco Fontgalland, and Leonardo Lorenzo Bravo Roger. Microwave sensor for liquid dielectric characterization based on metamaterial complementary split ring resonator. *IEEE Sensors Journal*, 18(24):9978–9983, 2018.

[78] Mark K Krage and George I Haddad. Frequency-dependent characteristics of microstriptransmission lines. *IEEE Transactions on Microwave Theory and Techniques*, 20(10):678–688, 1972.

[79] Spartak S Gevorgian, Torsten Martinsson, Peter LJ Linner, and Erik Ludvig Kollberg. Cad models for multilayered substrate interdigital capacitors. *IEEE Transactions on microwave theory and techniques*, 44(6):896–904, 1996.

[80] Peter H Aaen, Jaime A Plá, and Constantine A Balanis. On the development of cad techniques suitable for the design of high-power rf transistors. *IEEE transactions on microwave theory and techniques*, 53(10):3067–3074, 2005.

[81] Alexander V Mamishev, Kishore Sundara-Rajan, Fumin Yang, Yanqing Du, and Markus Zahn. Interdigital sensors and transducers. *Proceedings of the IEEE*, 92(5):808–845, 2004.

[82] Analog Devices, Inc. *Wideband Synthesizer with Integrated VCO*, 2017. Rev. A.

[83] Analog Devices, Inc. *1 MHz to 8 GHz, 70 dB Logarithmic Detector/Controller*, 2017. Rev. D.

[84] Kamil Staszek, Slawomir Gruszczynski, and Krzysztof Wincza. Six-port reflectometer providing enhanced power distribution. *IEEE Transactions on Microwave Theory and Techniques*, 64(3):939–951, 2016.

[85] Kamel Haddadi and Tuami Lasri. Forward v-band vector network analyzer based on a modified six-port technique. In *2015 IEEE Topical Conference on Wireless Sensors and Sensor Networks (WiSNet)*, pages 23–25. IEEE, 2015.

[86] Kihyun Kim, Namgon Kim, Sung-Hyun Hwang, Yong-Kweon Kim, and Youngwoo Kwon. A miniaturized broadband multi-state reflectometer integrated on a silicon mems probe for complex permittivity measurement of biological material. *IEEE transactions on microwave theory and techniques*, 61(5):2205–2214, 2013.

[87] Gabor Vinci, Stefan Lindner, Francesco Barbon, Sebastian Mann, Maximilian Hofmann, Alexander Duda, Robert Weigel, and Alexander Koelpin. Six-port radar sensor for remote respiration rate and heartbeat vital-sign monitoring. *IEEE Transactions on Microwave Theory and Techniques*, 61(5):2093–2100, 2013.

[88] K Haddadi, MM Wang, C Loyez, D Glay, and Tuami Lasri. Four-port communication receiver with digital iq-regeneration. *IEEE microwave and wireless components letters*, 20(1):58–60, 2009.

[89] K Haddadi, MM Wang, D Glay, and T Lasri. Ultra wide-band four-port reflectometer using only two quadratic detectors. In *2008 IEEE MTT-S International Microwave Symposium Digest*, pages 379–382. IEEE, 2008.